International Journal of Control

ISSN: 0020-7179 (Print) 1366-5820 (Online) Journal homepage: http://www.tandfonline.com/loi/tcon20

Grey-box state-space identification of nonlinear mechanical vibrations

J. P. Noël & J. Schoukens

To cite this article: J. P. Noël & J. Schoukens (2017): Grey-box state-space identification of nonlinear mechanical vibrations, International Journal of Control, DOI: 10.1080/00207179.2017.1308557

To link to this article: http://dx.doi.org/10.1080/00207179.2017.1308557

Accepted author version posted online: 23 Mar 2017.
Published online: 10 Apr 2017.

INTERNATIONAL JOURNAL OF CONTROL, 2017
https://doi.org/10.1080/00207179.2017.1308557

Taylor & Francis
Taylor & Francis Group

Grey-box state-space identification of nonlinear mechanical vibrations

J. P. Noël[a,b] and J. Schoukens[b]

[a]Space Structures and Systems Laboratory, Aerospace and Mechanical Engineering Department, University of Liège, Liège, Belgium; [b]ELEC Department, Vrije Universiteit Brussel, Brussels, Belgium

ABSTRACT

The present paper deals with the identification of nonlinear mechanical vibrations. A grey-box, or semi-physical, nonlinear state-space representation is introduced, expressing the nonlinear basis functions using a limited number of measured output variables. This representation assumes that the observed nonlinearities are localised in physical space, which is a generic case in mechanics. A two-step identification procedure is derived for the grey-box model parameters, integrating nonlinear subspace initialisation and weighted least-squares optimisation. The complete procedure is applied to an electrical circuit mimicking the behaviour of a single–input, single–output (SISO) nonlinear mechanical system and to a single–input, multiple–output (SIMO) geometrically nonlinear beam structure.

ARTICLE HISTORY
Received 15 February 2016
Accepted 14 March 2017

KEYWORDS
Nonlinear system identification; nonlinear mechanical vibrations; grey-box modelling; semi-physical modelling; state-space equations; Silverbox benchmark; nonlinear beam benchmark

1. Introduction

Operating in nonlinear regime has become a popular design solution for many systems and devices in order to meet escalating performance requirements. Among a variety of potential examples, the nonlinear implementation of signal processing operations is worthy of mention. In Boechler, Theocharis, and Daraio (2011), tunable rectification was achieved using a granular crystal with bifurcating dynamics leading to quasiperiodic and chaotic states. By coupling nonlinear modes through internal resonances, Antonio, Zanette, and Lopez (2012) proposed a frequency stabilisation mechanism for micromechanical resonators. In Strachan, Shaw, and Kogan (2013), a chain of nonlinear resonators involving a cascade of parametric resonances was also used to passively divide frequencies. In the field of mechanical vibrations, intentionally utilising nonlinearity has similarly attracted a great deal of attention over the past few years, in particular for devising vibration absorbers (Habib & Kerschen, 2015; Wierschem et al., 2017) and harvesters (Karami & Inman, 2012).

This emergence of ever-more complicated nonlinear designs calls for the development of a new generation of data-driven modelling tools capable of accounting for nonlinear phenomena. The most recent and popular contributions pursuing this goal in mechanical vibration engineering were surveyed in Noël and Kerschen (2017), and include, e.g. nonlinear modal analysis techniques (Chen et al., 2014; Noël, Renson, Grappasonni, & Kerschen, 2016; Peeters, Kerschen, & Golinval, 2011; Renson, Gonzalez-Buelga, Barton, & Neild, 2016) and numerical model updating methods (Claeys, Sinou, Lambelin, & Alcoverro, 2014; Isasa, Hot, Cogan, & Sadoulet-Reboul, 2011).

One of the major challenges in nonlinear data-driven modelling, or nonlinear system identification, is to address the constant compromise existing between the flexibility of the fitted model and its parsimony. Flexibility refers to the ability of the model to capture complex nonlinearities, while parsimony is its quality to possess a low number of parameters. In this paper, we concentrate on nonlinear state-space representations of the kind

$$\begin{cases} \dot{\mathbf{x}}(t) = \mathbf{A}\,\mathbf{x}(t) + \mathbf{B}\,\mathbf{u}(t) + \mathbf{E}\,\mathbf{g}(\mathbf{x}, \mathbf{u}, \mathbf{y}) \\ \mathbf{y}(t) = \mathbf{C}\,\mathbf{x}(t) + \mathbf{D}\,\mathbf{u}(t) + \mathbf{F}\,\mathbf{h}(\mathbf{x}, \mathbf{u}, \mathbf{y}), \end{cases} \tag{1}$$

which can be classified as very flexible but little parsimonious, two features typically shared by black-box models. In Equation (1), $\mathbf{A} \in \mathbb{R}^{n_s \times n_s}$, $\mathbf{B} \in \mathbb{R}^{n_s \times m}$, $\mathbf{C} \in \mathbb{R}^{l \times n_s}$ and $\mathbf{D} \in \mathbb{R}^{l \times m}$ are the linear state, input, output and direct feedthrough matrices, respectively; $\mathbf{x}(t) \in \mathbb{R}^{n_s}$ is the state vector; $\mathbf{y}(t) \in \mathbb{R}^{l}$ and $\mathbf{u}(t) \in \mathbb{R}^{m}$ are the output and input vectors, respectively. The linear-in-the-parameters expressions $\mathbf{E}\,\mathbf{g}(\mathbf{x}, \mathbf{u}, \mathbf{y}) \in \mathbb{R}^{n_s}$ and $\mathbf{F}\,\mathbf{h}(\mathbf{x}, \mathbf{u}, \mathbf{y}) \in \mathbb{R}^{l}$ are the nonlinear model terms coupling the state, input and output variables. The order of the model, i.e. the dimension of the state space, is denoted as n_s.

In the analysis of mechanical vibrations, one very often distinguishes nonlinearities distributed throughout (some large region of) the entire structure from localised

CONTACT J. P. Noël jp.noel@ulg.ac.be

nonlinearities, which are physically confined to a small area. Localised nonlinearities are arguably the most common in mechanical engineering practice, as they typically arise in joints interfacing substructures. Meaningful examples of this reality can be found in aerospace applications. During the modal survey of the Cassini spacecraft (Carney, Yunis, Smith, & Peng, 1997), nonlinearities resulting from the appearance of gaps in the truss supports of the Huygens probe were attested. Similarly, the analysis of in-orbit data of the International Space Station highlighted that the opening of a pin connection in the assembly of its solar arrays led to severe nonlinear manifestations (Laible, Fitzpatrick, & Grygier, 2013). Nonlinearities were also reported during ground vibration testing of the Airbus A400M, and were attributed to the elastomeric mounts supporting the four turboprop engines of the aircraft (Ahlquist, Carreño, Climent, de Diego, & de Alba, 2010).

In the present paper, it is shown that, in the case of mechanical systems where nonlinearities are localised in physical space, the black-box model structure in Equation (1) can be drastically simplified. More specifically, Section 2 demonstrates that the nonlinear terms in Equation (1) can be constructed using a limited number of output measurements, and hence without involving the state and input vectors. This makes the resulting grey-box state-space model a parsimonious representation of nonlinear mechanical systems. A two-step identification procedure is derived for this model in Section 3, integrating nonlinear subspace initialisation and weighted least-squares optimisation. Finally, the complete procedure is applied in Sections 4 and 5 to an electrical circuit mimicking the behaviour of a single–input, single–output (SISO) nonlinear mechanical system and to a single–input, multiple–output (SIMO) geometrically nonlinear beam structure, respectively.

2. Grey-box state-space modelling based on Newton's second law

Assuming localised nonlinearities, the vibrations of a n_p-degree-of-freedom mechanical system, i.e. a system featuring n_p linear resonances, obey Newton's second law written in the form

$$\mathbf{M}\,\ddot{\mathbf{y}}(t) + \mathbf{C}_v\,\dot{\mathbf{y}}(t) + \mathbf{K}\,\mathbf{y}(t) + \sum_{a=1}^{s} c_a\,\mathbf{g}_a(\mathbf{y}_{nl}(t), \dot{\mathbf{y}}_{nl}(t)) = \mathbf{u}(t), \tag{2}$$

where $\mathbf{M}$, $\mathbf{C}_v$, $\mathbf{K} \in \mathbb{R}^{n_p \times n_p}$ are the mass, linear viscous damping and linear stiffness matrices, respectively; $\mathbf{y}(t)$, $\dot{\mathbf{y}}(t)$, $\ddot{\mathbf{y}}(t)$ and $\mathbf{u}(t) \in \mathbb{R}^{n_p}$ are the displacement, velocity, acceleration and external force vectors, respectively; the nonlinear restoring force term is formed as the sum of s basis function vectors $\mathbf{g}_a(t) \in \mathbb{R}^{n_p}$ associated with coefficients c_a. The subsets of displacements and velocities involved in the construction of the basis functions are denoted $\mathbf{y}_{nl}(t)$ and $\dot{\mathbf{y}}_{nl}(t)$, respectively. To fix ideas and illustrate Equation (2), the 2-degree-of-freedom mechanical system shown in Figure 1 is considered. It comprises one cubic stiffness element, and obeys Newton's law as written term-by-term in Equation (3). Because the nonlinearity in the system is localised between mass 2 and a fixed base, vector $\mathbf{g}_1 = (\,0\;y_2^3\,)^T$ in Equation (3) possesses a single nonzero element function of $y_{nl} = y_2$.

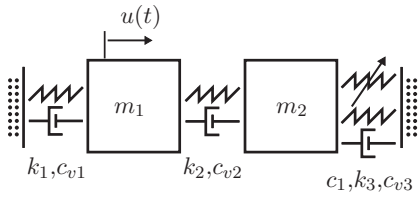

Figure 1. An illustrative 2-degree-of-freedom mechanical system with one localised nonlinearity.

$$\begin{pmatrix} m_1 & 0 \\ 0 & m_2 \end{pmatrix}\begin{pmatrix} \ddot{y}_1 \\ \ddot{y}_2 \end{pmatrix} + \begin{pmatrix} c_{v1}+c_{v2} & -c_{v2} \\ -c_{v2} & c_{v2}+c_{v3} \end{pmatrix}\begin{pmatrix} \dot{y}_1 \\ \dot{y}_2 \end{pmatrix} + \begin{pmatrix} k_1+k_2 & -k_2 \\ -k_2 & k_2+k_3 \end{pmatrix}\begin{pmatrix} y_1 \\ y_2 \end{pmatrix} + c_1\begin{pmatrix} 0 \\ y_2^3 \end{pmatrix} = \begin{pmatrix} u(t) \\ 0 \end{pmatrix} \tag{3}$$

The dynamics governed by Equation (2) is conveniently interpreted by moving the nonlinear restoring force term to the right-hand side, i.e.

$$\mathbf{M}\,\ddot{\mathbf{y}}(t) + \mathbf{C}_v\,\dot{\mathbf{y}}(t) + \mathbf{K}\,\mathbf{y}(t) = \mathbf{u}(t) - \sum_{a=1}^{s} c_a\,\mathbf{g}_a(\mathbf{y}_{nl}(t), \dot{\mathbf{y}}_{nl}(t)), \tag{4}$$

which leads to the block-diagram representation in Figure 2.

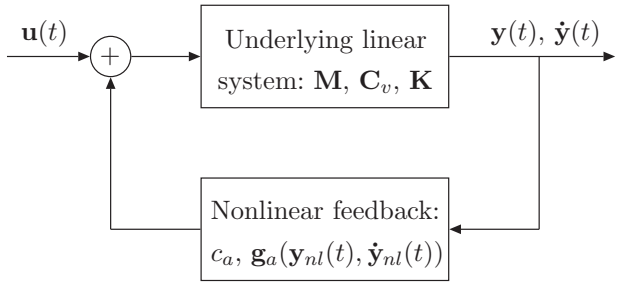

Figure 2. Feedback interpretation of Newton's law in Equation (2).

The feedback structure of this diagram suggests that localised nonlinearities in mechanical systems act as additional inputs applied to the underlying linear system. This, in turn, reveals that black-box nonlinear terms in a state-space model, such as $\mathbf{E}\,\mathbf{g}(\mathbf{x},\mathbf{u},\mathbf{y})$ and $\mathbf{F}\,\mathbf{h}(\mathbf{x},\mathbf{u},\mathbf{y})$ in Equations (1), are overly complex to address mechanical vibrations. A more parsimonious description of nonlinearities is achieved by translating Equation (4) in state space, which provides the grey-box model

$$\begin{cases} \dot{\mathbf{x}}(t) = \mathbf{A}\,\mathbf{x}(t) + \mathbf{B}\,\mathbf{u}(t) + \mathbf{E}\,\mathbf{g}(\mathbf{y}_{nl}(t), \dot{\mathbf{y}}_{nl}(t)) \\ \mathbf{y}(t) = \mathbf{C}\,\mathbf{x}(t) + \mathbf{D}\,\mathbf{u}(t) + \mathbf{F}\,\mathbf{g}(\mathbf{y}_{nl}(t), \dot{\mathbf{y}}_{nl}(t)), \end{cases} \tag{5}$$

where $\mathbf{g}(t) \in \mathbb{R}^s$ is a vector concatenating the nonzero elements in the basis function vectors $\mathbf{g}_a(t)$, and $\mathbf{E} \in \mathbb{R}^{n_x \times s}$ and $\mathbf{F} \in \mathbb{R}^{n_p \times s}$ are the associated coefficient matrices.

For the sake of conciseness, one adopts the concatenated equations

$$\begin{cases} \dot{\mathbf{x}}(t) = \mathbf{A}\,\mathbf{x}(t) + \overline{\mathbf{B}}\,\overline{\mathbf{u}}(t) \\ \mathbf{y}(t) = \mathbf{C}\,\mathbf{x}(t) + \overline{\mathbf{D}}\,\overline{\mathbf{u}}(t), \end{cases} \tag{6}$$

where $\overline{\mathbf{B}} = [\mathbf{B}\ \mathbf{E}]$ and $\overline{\mathbf{D}} = [\mathbf{D}\ \mathbf{F}]$; the extended input vector $\overline{\mathbf{u}}(t)$ is similarly defined as $[\mathbf{u}(t)^T\ \ \mathbf{g}(t)^T]^T$, where T is the transpose operation.

3. Identification procedure

The simplified structure of the grey-box state-space model proposed in Equation (6) lends itself to a two-step identification procedure, whereas four steps including two nonlinear optimisation searches are needed in classical black-box state-space identification (Paduart et al., 2010). First, initial estimates of the $\mathbf{A}$, $\overline{\mathbf{B}}$, $\mathbf{C}$ and $\overline{\mathbf{D}}$ matrices are obtained using nonlinear subspace identification. Second, the quality of the initial subspace parameter estimates is improved using nonlinear optimisation. The complete procedure is carried out in the frequency domain, opening the possibility to apply user-defined weighting functions in specific frequency intervals. We also opt for a discrete-time formulation to ensure a proper conditioning of the identification algorithm and to permit effective model-based time simulations.

3.1 Initial state-space model obtained using nonlinear subspace identification

Equation (6) is first recast in the frequency domain as

$$\begin{cases} z_k\,\mathbf{X}(k) = \mathbf{A}\,\mathbf{X}(k) + \overline{\mathbf{B}}\,\overline{\mathbf{U}}(k) \\ \mathbf{Y}(k) = \mathbf{C}\,\mathbf{X}(k) + \overline{\mathbf{D}}\,\overline{\mathbf{U}}(k), \end{cases} \tag{7}$$

where k is the frequency line, z_k the z-transform variable, and $\mathbf{Y}(k)$, $\mathbf{X}(k)$ and $\overline{\mathbf{U}}(k)$ the discrete Fourier transforms (DFTs) of $\mathbf{y}(t)$, $\mathbf{x}(t)$ and $\overline{\mathbf{u}}(t)$, respectively.

Initial estimates of the $(\mathbf{A}, \overline{\mathbf{B}}, \mathbf{C}, \overline{\mathbf{D}})$ matrices are calculated using the frequency-domain nonlinear subspace identification (FNSI) method proposed in Noël and Kerschen (2013). This method derives parameters non-iteratively from data by manipulating Equation (7) using geometric projections, and by considering the measured outputs as nonlinear regressors. The strength of using nonlinear subspace identification is that a fully nonlinear grey-box model is initially obtained, contrasting with the linearised initial model considered in the black-box state-space identification approach of Paduart et al. (2010). A complete description of the FNSI algorithm is provided in Appendix 1.

3.2 Final state-space model obtained using nonlinear optimisation

The recourse to measured outputs as regressors in the FNSI method causes parameter estimates to suffer from a systematic error, which magnitude depends on the output signal-to-noise ratio (SNR). To reduce this error, the second step of the identification procedure consists in minimising a weighted least-squares cost function with respect to all parameters in $\left(\mathbf{A}, \overline{\mathbf{B}}, \mathbf{C}, \overline{\mathbf{D}}\right)$.

3.2.1 Definition of the cost function

Introducing the vector of model parameters $\boldsymbol{\theta} \in \mathbb{R}^{n_\theta}$ as

$$\boldsymbol{\theta} = \left[vec\left(\mathbf{A}\right);\ vec\left(\overline{\mathbf{B}}\right);\ vec\left(\mathbf{C}\right);\ vec\left(\overline{\mathbf{D}}\right)\right], \tag{8}$$

where the operation denoted vec stacks the columns of a matrix on top of each other, the cost function to minimise writes

$$\mathbf{V}(\boldsymbol{\theta}) = \sum_{k=1}^{F} \boldsymbol{\epsilon}^H(k,\boldsymbol{\theta})\,\mathbf{W}(k)\,\boldsymbol{\epsilon}(k,\boldsymbol{\theta}), \tag{9}$$

where F is the number of processed frequency lines, H the Hermitian transpose, and $\mathbf{W}(k)$ a weighting function. The model error vector $\boldsymbol{\epsilon} \in \mathbb{R}^l$, where l is in general the number of measured output variables, is defined as the complex-valued difference

$$\boldsymbol{\epsilon}(k,\boldsymbol{\theta}) = \mathbf{Y}_m(k,\boldsymbol{\theta}) - \mathbf{Y}(k), \tag{10}$$

where $\mathbf{Y}_m(k,\boldsymbol{\theta})$ and $\mathbf{Y}(k)$ are the DFTs of the modelled and measured outputs, respectively.

3.2.2 Assumption on noise disturbances and weighting strategy

An output error framework is adopted according to the two following assumptions on the frequency-domain input and output noise disturbances.

Assumption 3.1 *The input spectrum is assumed to be noiseless, i.e. observed without errors and independent of the output noise. In practice, electromagnetic shakers used in mechanical applications typically yield SNRs of* 60–80 *dB, which is coherent with a noise-free assumption. If the input noise disturbances are otherwise too important, measurements can be averaged over multiple periods.*

Assumption 3.2: *The output disturbing noise term* $\mathbf{N}_Y(k)$ *is Gaussian distributed, has zero mean* $\mathcal{E}(\mathbf{N}_Y(k)) = 0$, *where* $\mathcal{E}$ *is the expectation operator, and has a covariance matrix with only nonzero diagonal elements equal to* $\boldsymbol{\sigma}_Y^2(k) = \mathcal{E}(|\mathbf{N}_Y(k)|^2)$, *as described in Schoukens, Pintelon, and Rolain* (1999).

In linear system identification, model errors are negligible relative to noise errors provided an adequate choice of the model order. In this case, the cost function $\mathbf{V}(\boldsymbol{\theta})$ in Equation (9) is usually weighted by the inverse of the noise magnitude, i.e. $\mathbf{W}(k) = \boldsymbol{\sigma}_Y^{-1}(k)$, leading to parameter estimates with maximum likelihood dispersion properties (Pintelon & Schoukens, 2001). In the presence of nonlinearities, model errors generally prevail over noise errors. Accordingly, we select herein a unitary weighting matrix $\mathbf{W}(k)$, assuming that unmodelled dynamics is uniformly distributed in the frequency domain.

3.2.3 Analytical calculation of the Jacobian matrix

In this work, the minimisation of the cost function $\mathbf{V}(\boldsymbol{\theta})$ in Equation (9) is performed by means of a Levenberg–Marquardt optimisation algorithm, which combines the large convergence region of the gradient descent method with the fast convergence of the Gauss–Newton method (Levenberg, 1944; Marquardt, 1963). This algorithm requires the calculation of the Jacobian matrix $\mathbf{J}(k, \boldsymbol{\theta})$ associated with the cost function or, equivalently, with the error function $\boldsymbol{\epsilon}(k, \boldsymbol{\theta})$, i.e.

$$\mathbf{J}(k, \boldsymbol{\theta}) = \frac{\partial \boldsymbol{\epsilon}(k, \boldsymbol{\theta})}{\partial \boldsymbol{\theta}} = \frac{\partial \mathbf{Y}_m(k, \boldsymbol{\theta})}{\partial \boldsymbol{\theta}}. \tag{11}$$

Given the nonlinear relationship which exists between $\mathbf{Y}(k)$ and $\overline{\mathbf{U}}(k)$ in Equation (7), it may not be practical to compute the elements of $\mathbf{J}(k, \boldsymbol{\theta})$ in the frequency domain. An alternative approach consists in carrying out the computation of the Jacobian matrix in the time domain, and then in applying the DFT. Following this idea, the analytical derivation of all elements in $\mathbf{J}(k, \boldsymbol{\theta})$ is achieved in Appendix 2.

Table 1. Natural frequency and damping ratio of the Silverbox benchmark estimated at 5 mV RMS.

Natural frequency (Hz)	Damping ratio (%)
68.58	4.68

4. Experimental demonstration on the Silverbox benchmark

The identification procedure described in Section 3 is demonstrated in the present section using experimental measurements acquired on the Silverbox benchmark, an electronic circuit mimicking the behaviour of a SISO mechanical system with a single resonance.

The system was excited using random phase multisines (Pintelon & Schoukens, 2001) with root-mean-squared (RMS) amplitudes of 5 and 100 mV. The input frequency spectrum was limited to 0–300 Hz, excluding the DC component, and considering a sampling frequency of 2441 Hz. Experiments were conducted over 30 periods of 8192 samples each, removing the first five periods to achieve steady-state conditions. Table 1 reports the underlying linear modal properties of the Silverbox estimated at 5 mV RMS. Figure 3 depicts frequency response functions (FRFs) measured at 5 and 100 mV RMS. At high excitation level, a shift of the resonance frequency of about 9 Hz together with severe nonlinearity-induced stochastic distortions is noticed.

4.1 Grey- versus black-box identification

The Silverbox was designed to exhibit the dynamics of a Duffing oscillator with cubic spring, though previous studies concluded that it also features an asymmetry in its nonlinear characteristic (Noël, Schoukens, & Kerschen, 2015; Schoukens, Nemeth, Crama, Rolain, & Pintelon, 2003). This is usually modelled using an additional quadratic stiffness term, prescribing the equation of motion

$$M\,\ddot{y}(t) + C_v\,\dot{y}(t) + K\,y(t) + c_1\,y^2(t) + c_2\,y^3(t) = u(t) \tag{12}$$

A state-space model of the Silverbox system, in the grey-box form of Equation (5), is constructed in discrete time at 100 mV RMS. According to the physical description given in Equation (12), nonlinear terms in the state equation are chosen to be quadratic and cubic functions of the measured output displacement $y_{nl}(t)$. The resulting vector $\boldsymbol{\theta}$ in Equation (8) contains 13 parameters, given a model order equal to 2. In Paduart et al. (2010), a black-box, second-order state-space model, in the discrete-time form equivalent to Equation (1), was identified

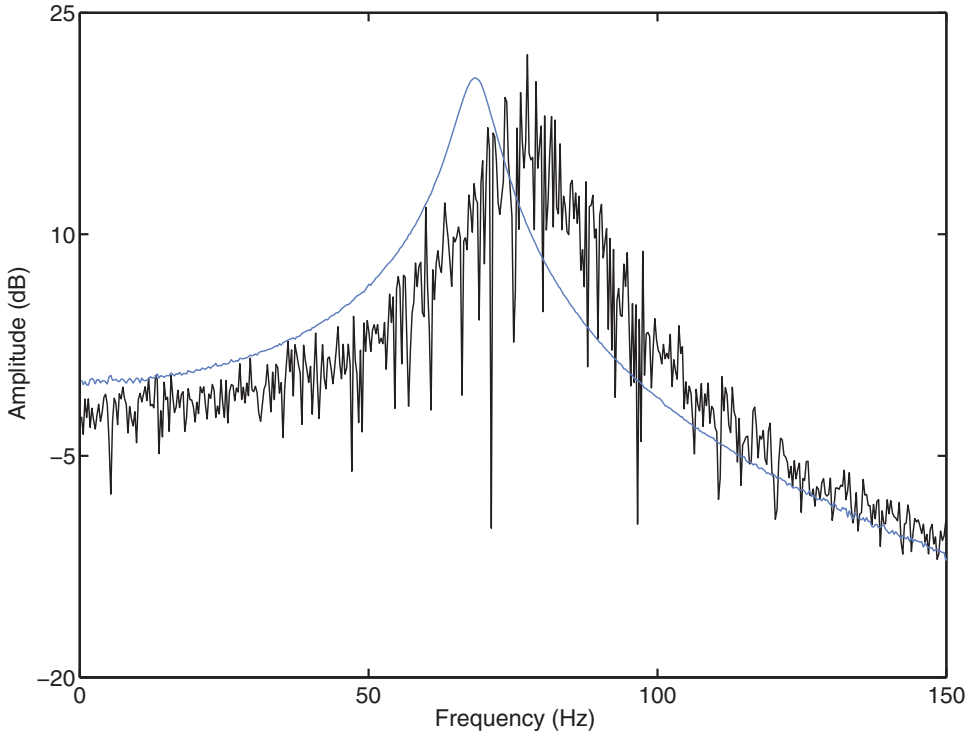

Figure 3. (Colour online) Comparison of FRFs measured at 5 (in blue) and 100 (in black) mV RMS.

considering a third-degree multivariate polynomial in the state equation with all cross products included, and linear terms only in the output equation. This led to a nonlinear model with 37 parameters.

The frequency-domain behaviour of the grey-box model error is studied in Figure 4(a), where the output spectrum in grey is compared with the initial and final state-space fitting error levels in orange and blue, respectively. The error of a linear state-space model is also plotted in green. Error levels were evaluated on a validation data set consisting of one period of 8192 samples measured at 100 mV RMS. The noise level displayed in black was obtained by averaging estimation data over the 25 periods acquired in steady state. The initial model obtained using nonlinear subspace identification (in orange) features a low error level, generally lying 40 dB below the output spectrum. This accuracy is explained by the high SNR of the output measurement (around 50 dB), which limits the systematic error discussed in Section 3.2. The final model error (in blue) closely matches the noise level in the resonance region, translating a virtually perfect fitting in this interval. A larger error is noticed around 250 Hz, which might be attributed to an unmodelled resonance between the fifth harmonic of the noise signal and the third harmonic of the Silverbox response. The time-domain errors corresponding to Figure 4(a) are depicted in Figure 4(b). The RMS values of the validation output time history and of the linear model error are equal to 0.16 and 0.09 V, respectively. The initial and final state-space models obtained following the identification procedure of Section 3 decrease this error down to 0.002 and 0.001 V, respectively.

Figure 5(a,b) compares in the frequency domain the proposed grey-box approach with the black-box identification method of Paduart et al. (2010). In Figure 5(a), initial model error spectra are superposed. The graph shows the clear advantage in starting from the nonlinear subspace model (in orange) described in Section 3.1, as opposed to the linearised model (in green) adopted in black-box identification. Final models are assessed in Figure 5(b). They are seen to lead to a similar validation error level, proving the accuracy of the introduced grey-box framework. The Levenberg–Marquardt iterations necessary to construct the final grey-box and black-box models are eventually analysed in Figure 6. It is observed that an optimal grey-box model is reached in a single iteration, whereas 33 iterations are required by the black-box model. This significant difference is the result of the already low initial error of the nonlinear subspace model (−55 dB), in comparison with the more substantial error of the linearised model (−21 dB).

4.2 Nonlinear coefficients and discrete- to continuous-time conversion

The coefficients of the physical system nonlinearities, i.e. c_1 and c_2 in Equation (12), can be calculated from the

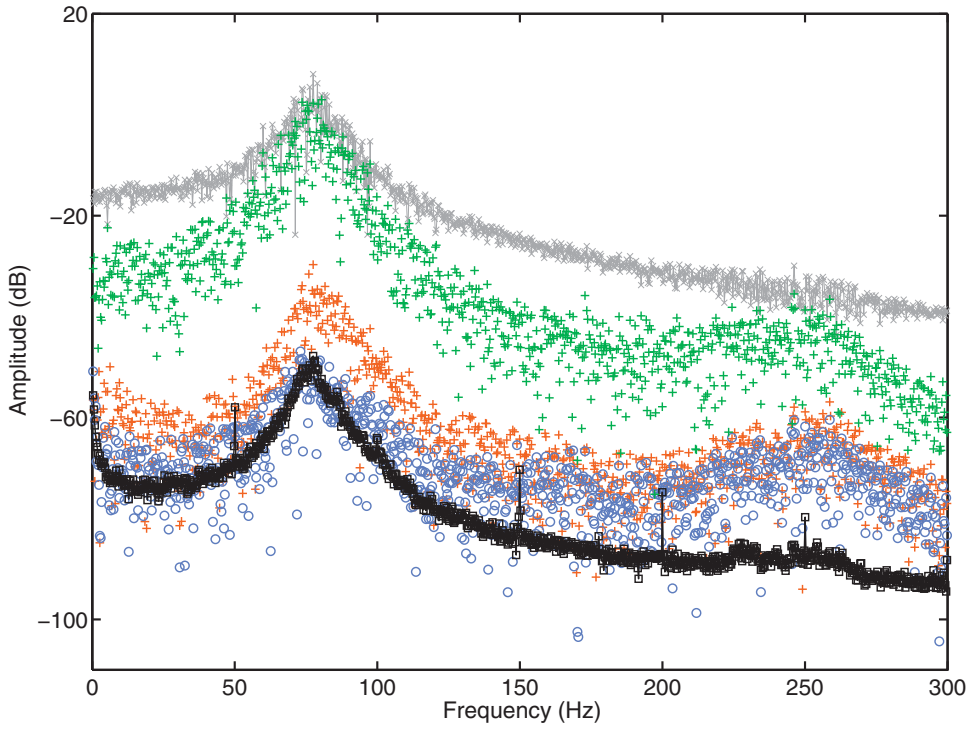

(a)

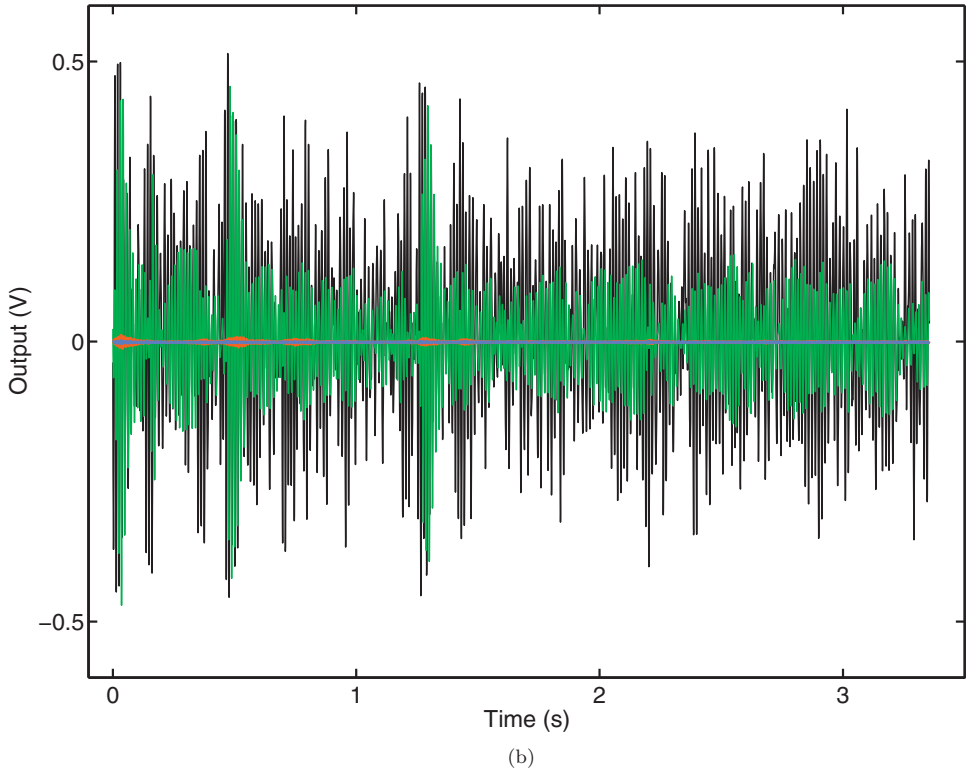

(b)

Figure 4. (Colour online) (a) Frequency-domain behaviour of the validation model error over the input band, featuring the output spectrum (in grey), linear state-space error level (in green), initial (in orange) and final (in blue) grey-box state-space error levels, and noise level (in black). (b) Time-domain validation plot, with the output time history (in black), linear state-space error (in green), and initial (in orange) and final (in blue) grey-box nonlinear state-space errors.

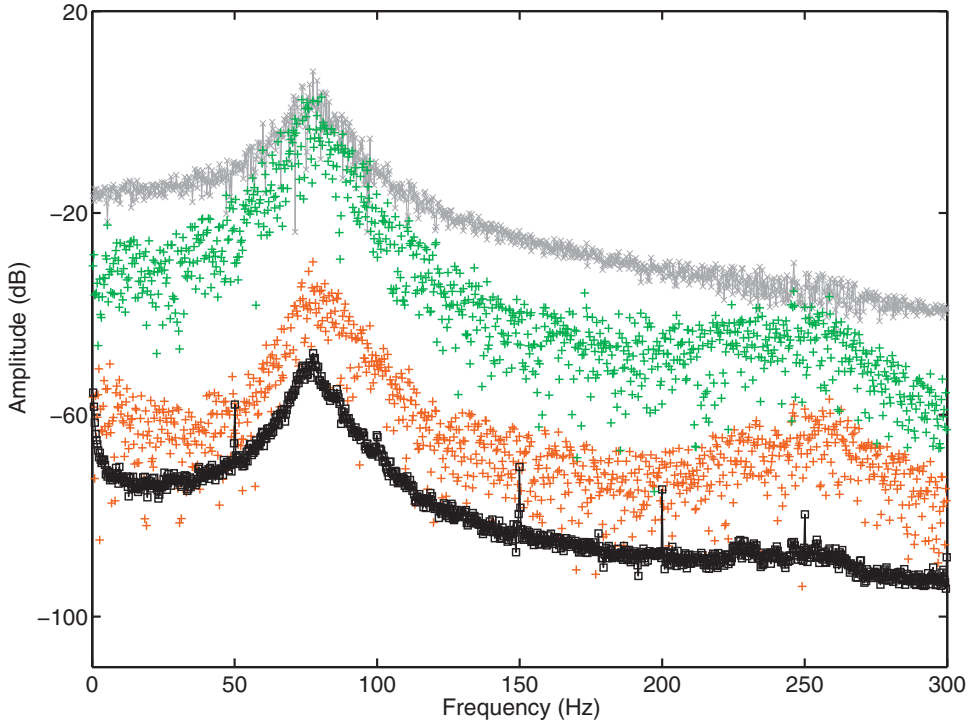

(a)

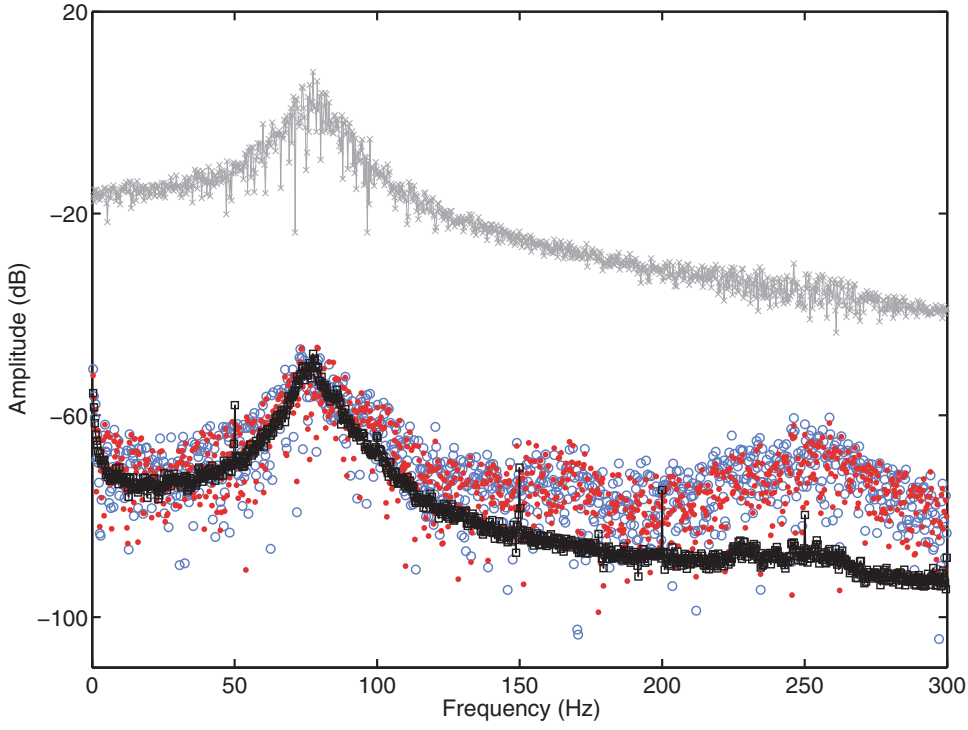

(b)

Figure 5. (Colour online) Frequency-domain comparison of the grey-box and black-box state-space modelling approaches. Validation output spectra and noise levels are plotted in grey and black, respectively. (a) Initial grey-box model obtained using nonlinear subspace identification (in orange) and initial linear black-box model (in green); (b) final grey-box (in blue) and black-box (in red) models.

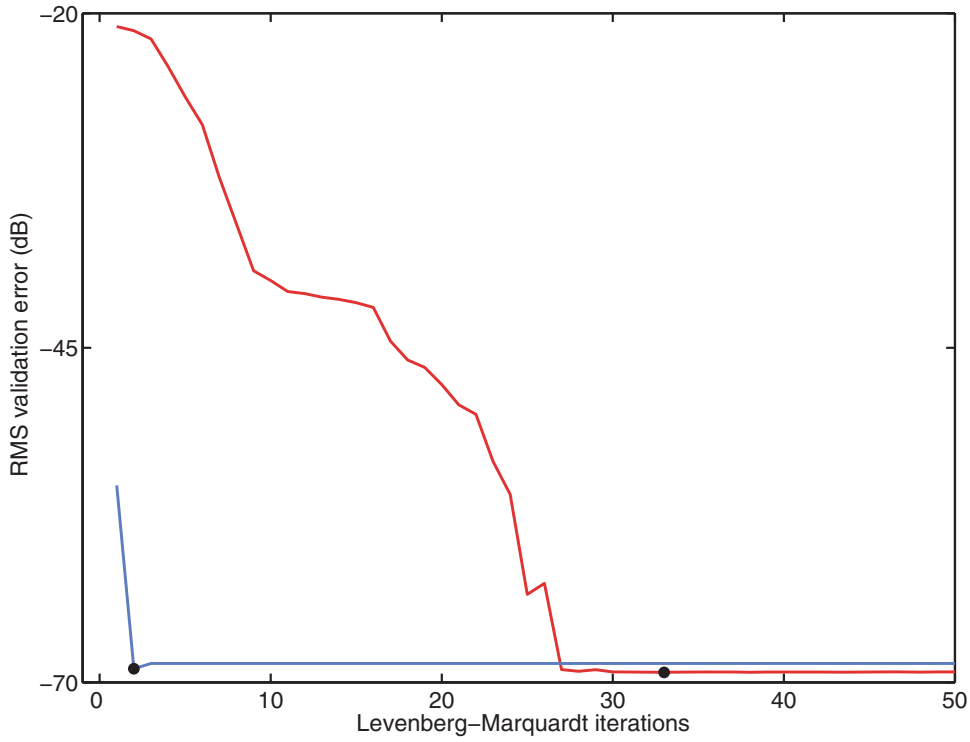

Figure 6. (Colour online) Decrease of the RMS validation error over 50 Levenberg–Marquardt iterations for the grey-box (in blue) and black-box (in red) approaches. Optimal models are located using black dots.

final estimates of the grey-box state-space parameters. Following the procedure described in Marchesiello and Garibaldi (2008), the generated nonlinear coefficients are frequency-dependent and possess a spurious imaginary part. They are obtained as the ratios of elements of the transfer function matrix associated with the model in Equation (7). This matrix is formed in continuous time, assuming zero-order-hold equivalence between the discrete- and continuous-time domains.

The real and imaginary parts of the estimated c_1 and c_2 are depicted versus frequency in Figure 7. They are presented for two distinct sampling frequencies, namely the original rate of 2441 Hz (in black) and a five-times greater rate of 12,205 Hz (in blue). The imaginary parts of the coefficients are seen to be more than one order of magnitude smaller than the real parts. The frequency dependence of the real parts is also found to be reduced when increasing the sampling frequency, as a result of the decrease of the error inherent to the discrete- to continuous-time conversion (Pintelon & Schoukens, 2001; Relan & Schoukens, 2016). Using the averaged values of the coefficients calculated at 2441 Hz (doing so at 12,205 Hz leads to very similar values, see Table 2), Figure 8 displays the synthesis of the nonlinear restoring force $c_1 y_{nl}^2(t) + c_2 y_{nl}^3(t)$ in the system. The cubic nonlinearity dominates this force–displacement curve, even though it additionally exhibits a slight asymmetry due to the quadratic nonlinearity, particularly visible in the close-up plot.

Table 2. Spectral average over the input band of the real parts of the nonlinear coefficients c_1 and c_2 for sampling frequencies of 2441 and 12,205 Hz.

Sampling frequency (Hz)	c_1 (SI)	c_2 (SI)
2441	−0.256	3.98
12,205	−0.267	3.96

4.3 Statistical analysis over multiple input realisations

In this section, a statistical analysis of the Silverbox identification is conducted. Table 3 lists the means and standard deviations of the 13 grey-box model parameters calculated over 50 input realisations, i.e. 50 multisine input signals with different phase spectra independently drawn from a uniform distribution on $[0, 2\pi)$ (Pintelon & Schoukens, 2001). One first observes in this table the reasonably low variability of all estimates. Compared to parameters in ($\mathbf{B}$, $\mathbf{C}$, $\mathbf{D}$, $\mathbf{E}$), the linear dynamic parameters in matrix $\mathbf{A}$ are also found to exhibit a ratio between standard deviation and mean values lower by one order of magnitude.

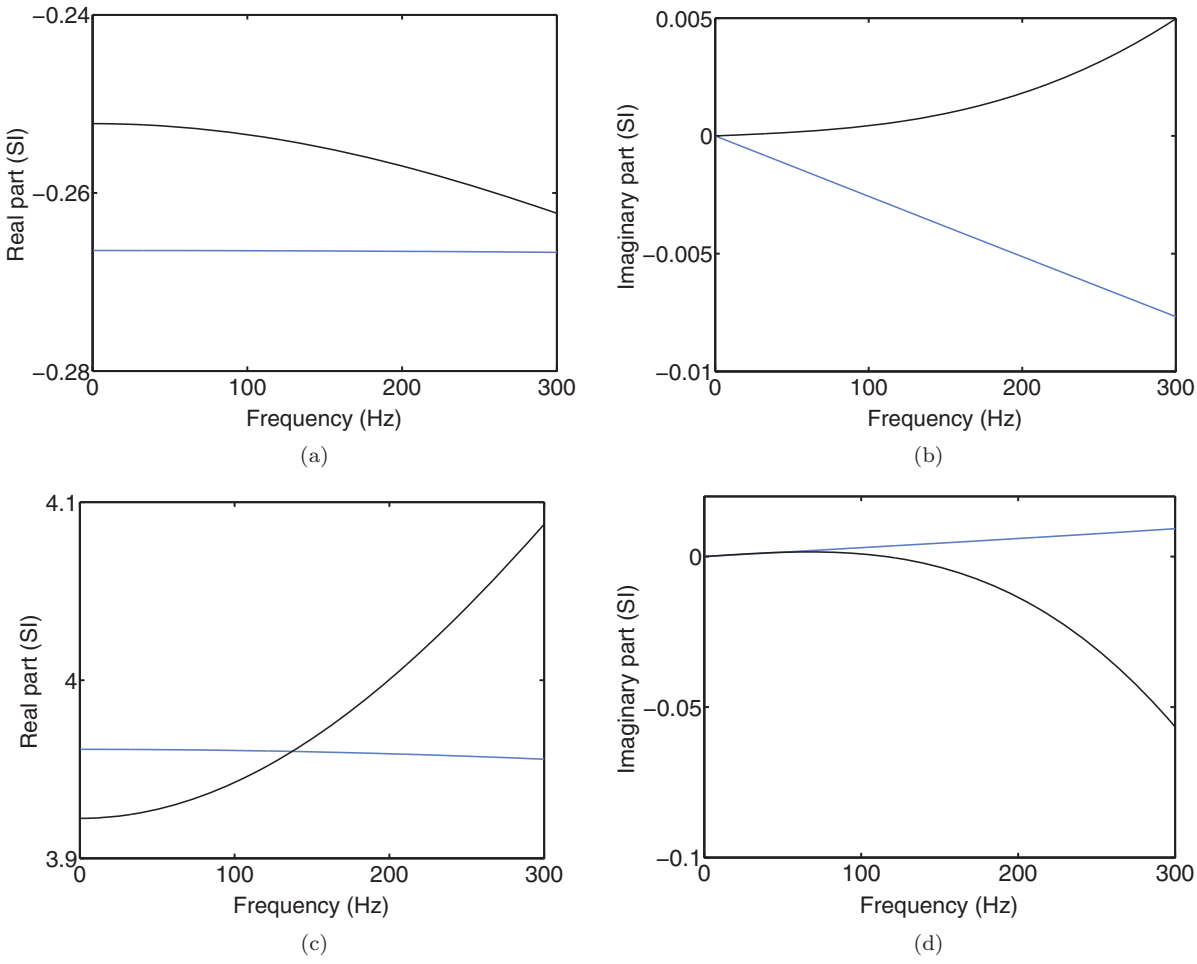

Figure 7. (Colour online) Complex-valued and frequency-dependent estimates of the nonlinear coefficients (a and b) c_1 and (c and d) c_2 for sampling frequencies of 2441 Hz (in black) and 12205 Hz (in blue).

In Table 4, similar statistics are given for the modal and physical parameters of the Silverbox system. The variability in the estimation of the linear natural frequency and damping ratio is marginal, although damping ratio estimates are seen to be comparatively more scattered. Similarly, the physical coefficient c_1 of the quadratic nonlinearity features a standard-deviation-over-mean ratio of −1.81 %, compared to 0.18 % for the cubic

Table 3. Statistics (means and standard deviations) of the 13 grey-box state-space parameters calculated over 50 input realisations. The ratios between standard deviation and mean values are also given in %.

Parameter	Mean (SI)	Standard deviation (× 100)	Std. dev./mean (%)
$A(1,1)$	0.97	0.47	0.49
$A(2,1)$	− 0.16	0.10	− 0.59
$A(1,2)$	0.19	0.11	0.58
$A(2,2)$	0.98	0.47	0.49
$B(1,1)$	− 0.05	0.41	− 7.88
$B(2,1)$	− 0.14	0.50	− 3.66
$C(1,1)$	− 1.12	3.26	− 2.90
$C(1,2)$	0.20	3.75	18.80
$D(1,1)$	0.003	0.04	13.47
$E(1,1)$	− 0.01	0.11	− 8.34
$E(2,1)$	− 0.04	0.15	− 4.25
$E(1,2)$	0.20	1.60	7.83
$E(2,2)$	0.54	2.01	3.71

Table 4. Statistics of the Silverbox modal and physical parameters calculated over 50 input realisations.

Parameter	Mean	Standard deviation ($\times$ 100)	Std. dev./mean (%)
Natural frequency	68.79 (*Hz*)	1.00	0.01
Damping ratio	4.91 (%)	0.6	0.12
c_1	$-$ 0.26 (SI)	0.48	$-$ 1.81
c_2	3.99 (SI)	0.72	0.18

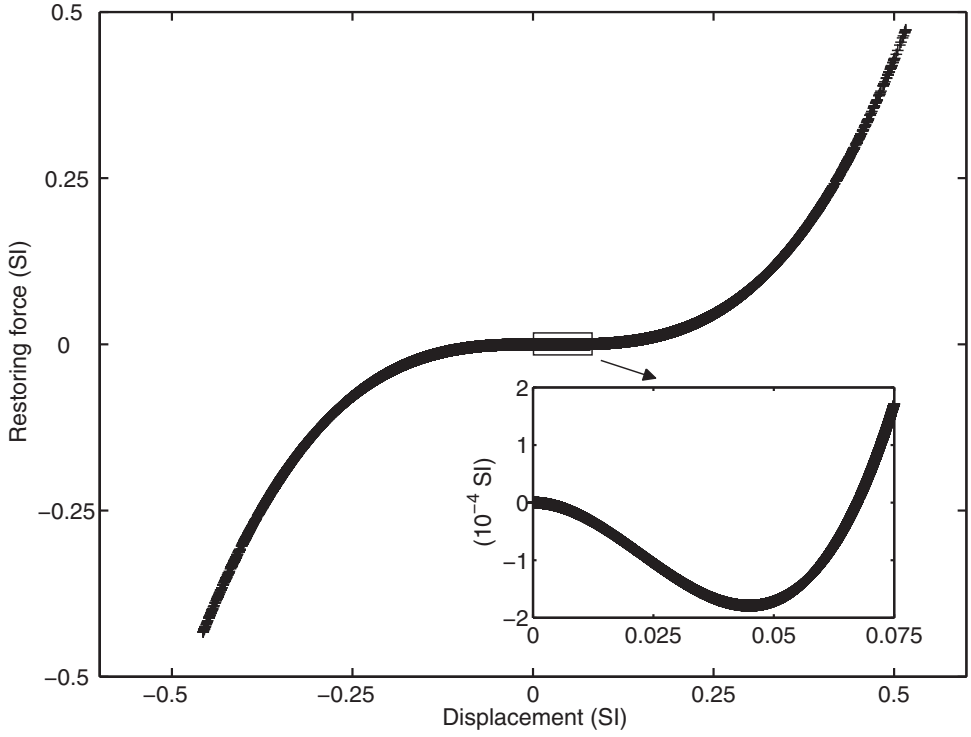

Figure 8. Silverbox nonlinear restoring force synthesised using the nonlinear coefficients averaged at 2441 Hz in Table 2.

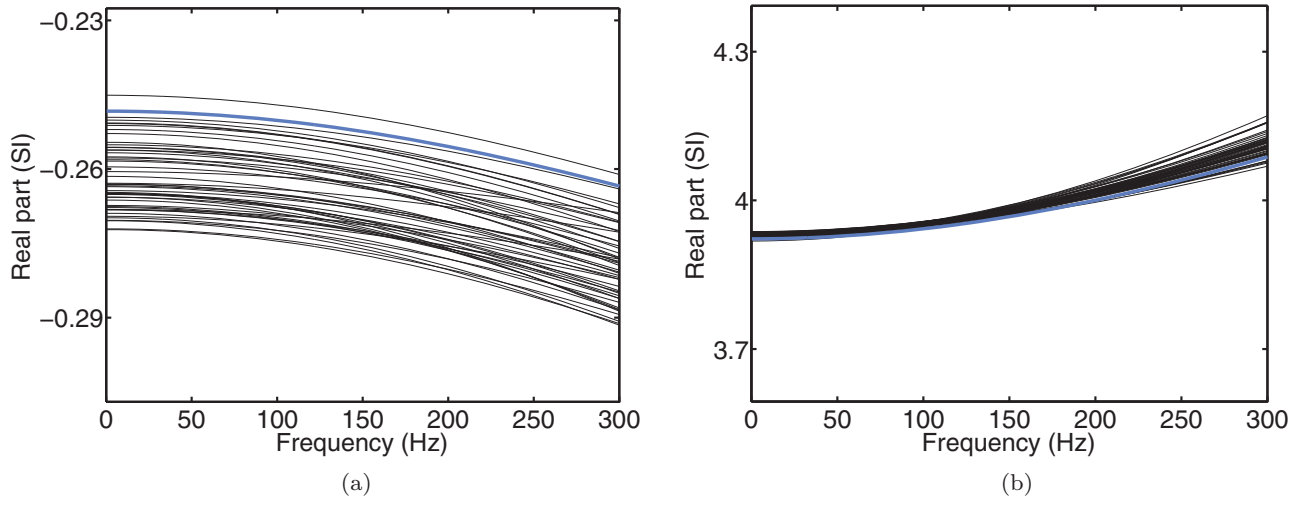

Figure 9. (Colour online) Variability of the frequency-dependent nonlinear coefficients (a) c_1 and (b) c_2 over 50 input realisations. In the two plots, the limits of the vertical axes correspond to $\pm$10% of the coefficient mean values. In blue, the two coefficients obtained in Section 4.2 are reproduced.

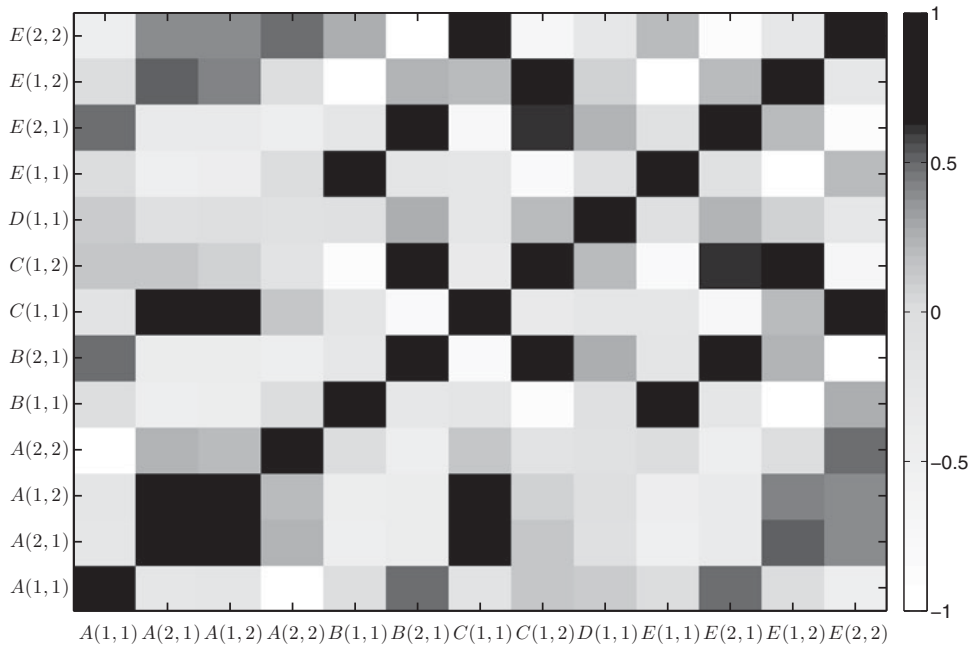

Figure 10. Correlation matrix of the 13 grey-box state-space parameters calculated over 50 input realisations.

coefficient. This is studied in Figure 9, where the 50 frequency-dependent estimates of c_1 and c_2 are depicted. In the two plots, the limits of the vertical axes correspond to $\pm 10\%$ of the coefficient mean values, confirming the greater variability of c_1.

The existence of correlation between the estimated state-space parameters is inspected in Figure 10. This figure presents the correlation matrix of the parameters, computed by normalising the rows and columns of their covariance matrix by the associated standard deviations. Multiple off-diagonal elements with significant magnitudes are observed, with five elements in the upper triangular block larger than 0.8. This is illustrated in Figure 11(a,b) by plotting the pairs of strongly correlated parameter estimates $\{A(2, 1), A(1, 2)\}$ (corr. $=$ 0.99) and $\{B(1, 1), E(1, 1)\}$ (corr. $=$ 0.97), respectively. The evidence of correlation implies that the derived state-space model is an overparametrised representation of the input–output relationship. In fact, Equation (12) indicates that five parameters in physical space are sufficient to describe the Silverbox dynamics, in comparison to the 13 grey-box parameters.

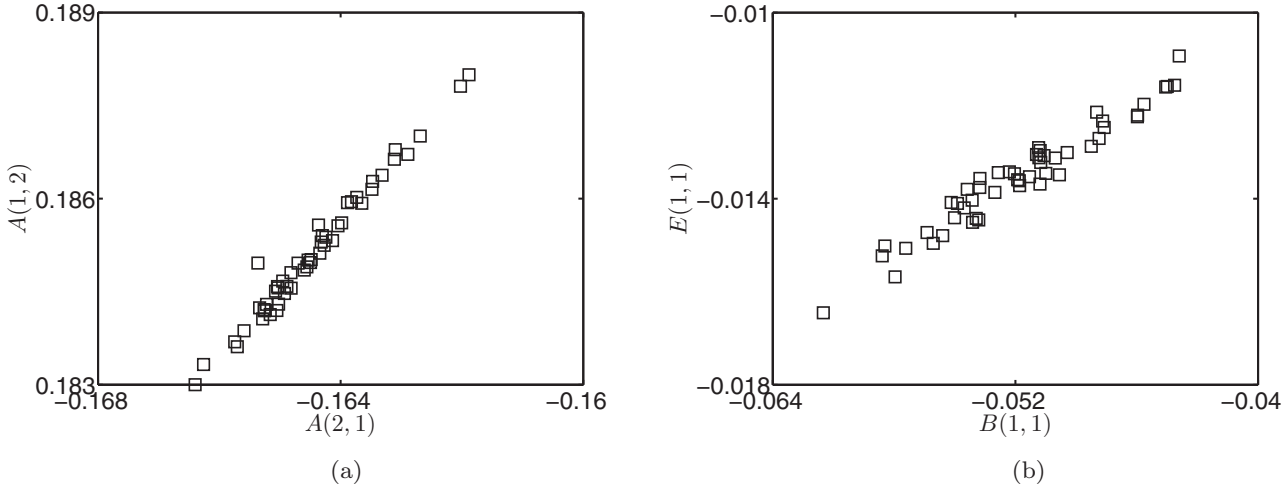

Figure 11. Evidence of the correlation existing between (a) the $A(2, 1)$ and $A(1, 2)$ parameters and (b) the $B(1, 1)$ and $E(1, 1)$ parameters.

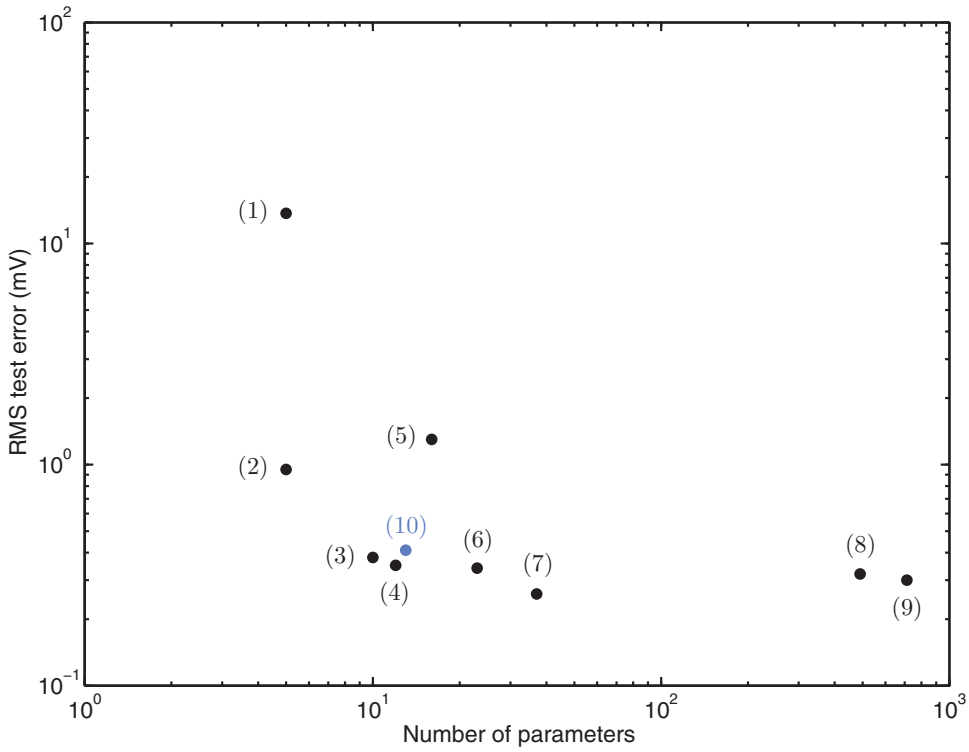

Figure 12. (Colour online) Comparison of 10 different nonlinear model structures based on benchmark data, namely (1) linear, (2) Hammerstein, (3) nonlinear feedback, (4) linear fractional representation, (5) locally linear state-space, (6) black-box state-space with sigmoidal nonlinearities, (7) black-box state-space with polynomial nonlinearities, (8) support vector machines, (9) neural network, and (10) grey-box state-space (this paper, in blue) models. Detailed information about the features of the different models is to be found in Marconato et al. (2012) and the references therein.

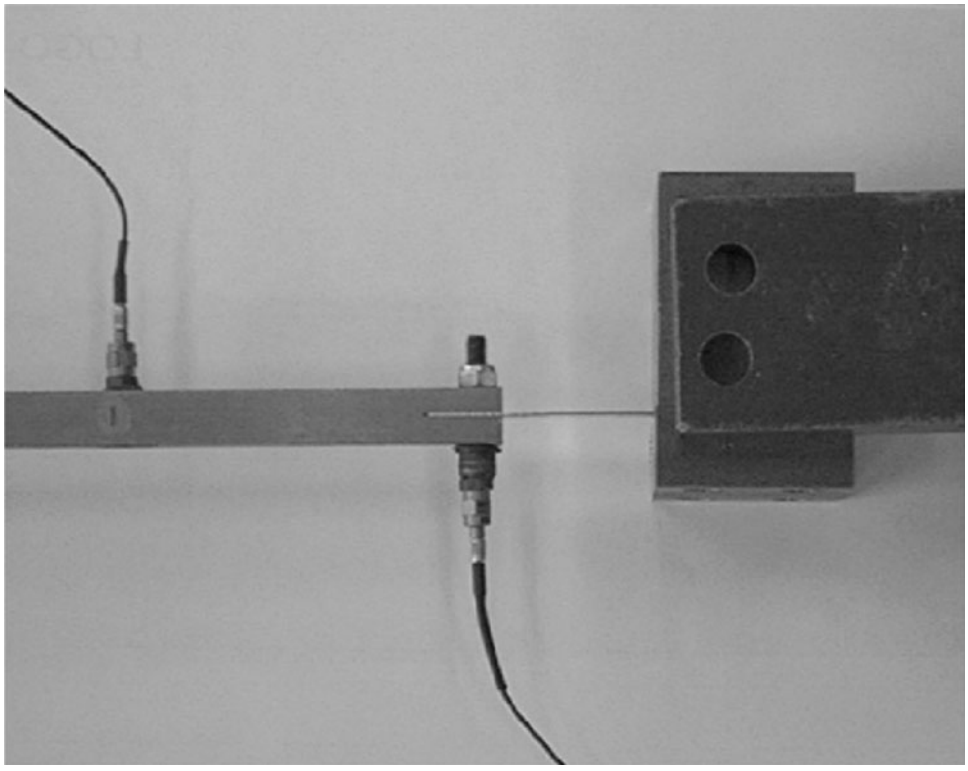

Figure 13. Close-up picture of the connection between the main linear beam and the thin beam (top view).

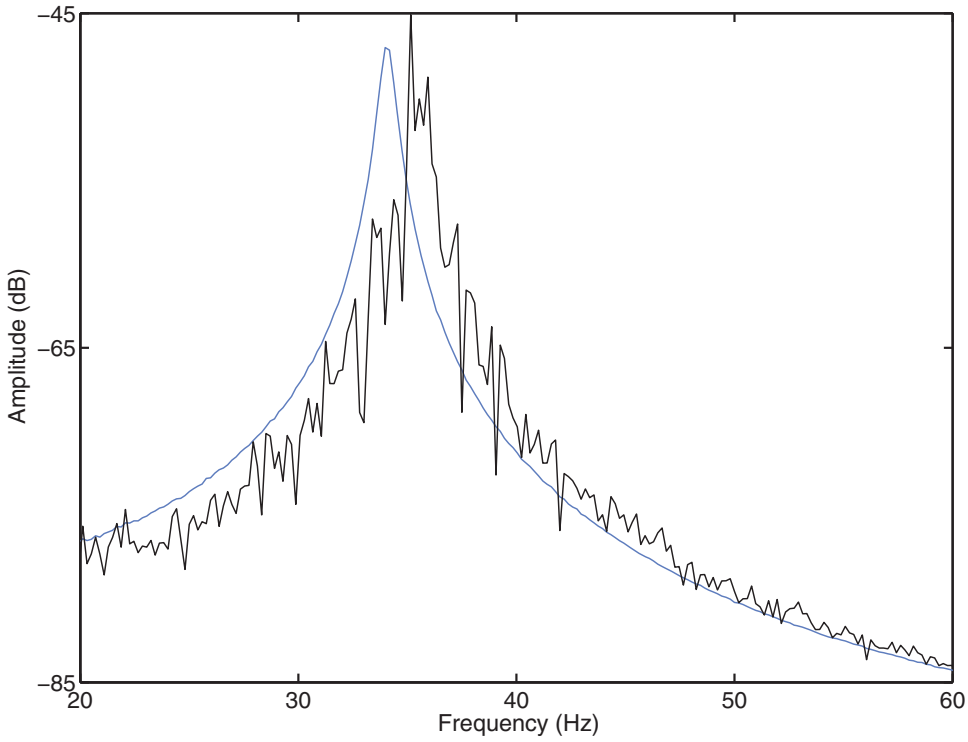

Figure 14. (Colour online) Comparison of FRFs measured at the main beam tip at 0.1 (in blue) and 1.2 (in black) V RMS.

It is a user decision to opt for a physical- or a state-space nonlinear modelling approach. Overparametrisation in state-space is expected to lead to a greater variability of the estimated parameters compared to a minimal system representation in physical space. However, in a grey-box formulation, the existence of correlation between state-space parameters results in physically interpretable parameters, namely linear modal properties and nonlinear coefficients, with little variability (see Table 4). Moreover, by increasing the model flexibility, overparametrising plays a key role in the decrease of the input–output simulation error (see Figure 4).

4.4 Comparison with other nonlinear model structures

The grey-box state-space model proposed in Section 2 is compared herein to a number of other nonlinear model structures. To this end, a benchmark data set measured on the Silverbox system, and described in Marconato, Sjöberg, Suykens, and Schoukens (2012), is utilised. It consists of 10 realisations of a multisine signal serving as estimation data, and of a filtered Gaussian noise sequence with increasing RMS value functioning as test data. In Figure 12, the RMS error evaluated on test data is plotted versus number of parameters for 10 different nonlinear models derived based on estimation data, namely (1) linear, (2) Hammerstein, (3) nonlinear feedback, (4) linear fractional representation, (5) locally linear state-space, (6) black-box state-space with sigmoidal nonlinearities, (7) black-box state-space with polynomial nonlinearities, (8) support vector machines, (9) neural network, and (10) grey-box state-space models. Detailed information about the features of the different models is to be found in Marconato et al. (2012) and the references therein. The model structure introduced in the present paper (number (10), in blue) is seen to achieve a good trade-off between accuracy and parsimony. It shows a slightly larger RMS error than black-box state-space models (numbers (6–7)), owing to the existence of an extrapolation region in the test data sequence where it fails to predict the Silverbox response accurately. However, it possesses the lowest number of parameters compared to other nonlinear state-space models (numbers (5–6–7)). It should finally be noted that models (2–3–4) are block-oriented models, which perform very well in the case of a SISO system with a single resonance but, unlike state-space models, generalise limitedly to larger scale systems with multiple resonances and nonlinearities.

5. Experimental demonstration on a nonlinear beam benchmark

This section demonstrates the identification procedure of Section 3 using the *Ecole Centrale de Lyon* (ECL) benchmark structure (Thouverez, 2003). It is an

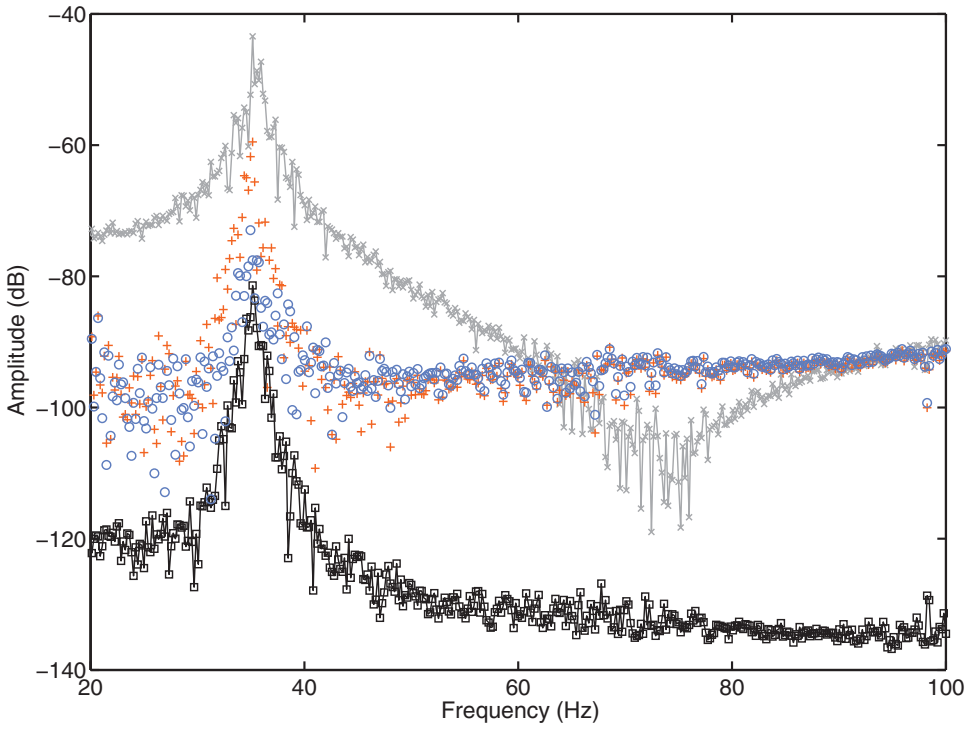

(a)

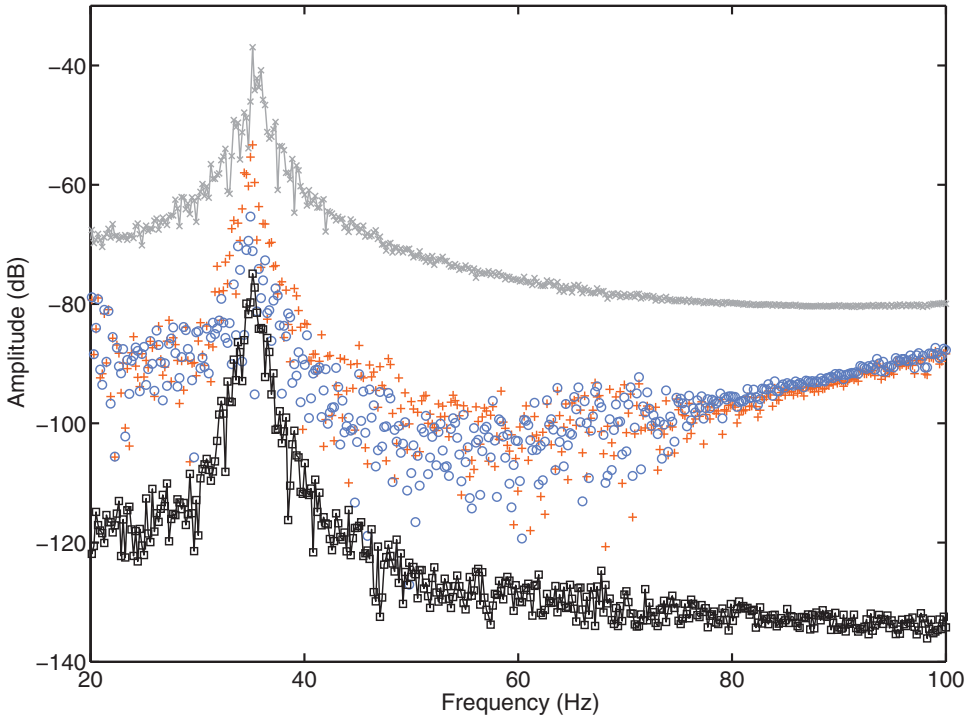

(b)

Figure 15. (Colour online) Frequency-domain behaviour of the validation model error over the 20–100 Hz band, featuring the output spectrum (in grey), initial (in orange) and final (in blue) grey-box state-space error levels, and noise level (in black). (a) Sensor 4 and (b) sensor 7.

experimental system comprising a thin beam behaving as a localised nonlinear stiffness component, connected to a linear thick beam with well-separated, lowly damped modes (see the geometric properties in Table 5). The system is clamped on both sides and is entirely made up of steel. A close-up picture of the connection between the main linear beam and the thin beam is displayed in Figure 13. The nature of the nonlinearity in the

Table 5. Geometric properties of the nonlinear beam benchmark.

Component	Length (m)	Width (mm)	Thickness (mm)
Main beam	0.7	14	14
Thin beam	0.04	14	0.5

Table 6. Linear natural frequency and damping ratio of the first structural mode of the nonlinear beam benchmark estimated at 0.1 V RMS.

Natural frequency (Hz)	Damping ratio (%)
34.08	1.11

Table 7. Spectral average over the 20–100 Hz band of the real parts of the nonlinear coefficients for a sampling frequency of 1600 Hz.

c_1 (SI)	c_2 (SI)	c_3 (SI)	c_4 (SI)
4.05×10^4	1.80×10^8	-4.46×10^{10}	-2.67×10^{13}

system is geometric, and is physically related to the substantially large displacements experienced by the thin beam at high forcing amplitude compared to its thickness.

The system was instrumented using seven accelerometers, regularly spaced along the main beam. Excitation signals were applied in a horizontal plane using a shaker connected to the main beam through a stinger attached 20 cm away from the clamping. An impedance head was used to measure force and acceleration signals at the excitation location. Random phase multisine inputs were generated, considering a sampling frequency of 1600 Hz and a frequency resolution of about 0.2 Hz (the number of time samples was 8192). The selected bandwidth of interest ranges from 20 to 100 Hz excluding DC and, in each experiment, 10 periods of input–output data were collected. The first two periods in each sequence were rejected to achieve steady state, and the final period was saved for validation. Because of dynamic interactions existing between the shaker and the structure, the input processed herein is the voltage signal measured at the output of the measurement setup amplifier.

At 0.1 V RMS input amplitude (corresponding approximately to 1.2 N RMS), the system exhibits linear dynamics, as expected from the geometric nature of the nonlinearity. The modal properties of the first structural mode estimated at this level are given in Table 6. Figure 14 compares FRFs measured at the main beam tip (sensor number 7) at 0.1 and 1.2 V RMS (corresponding approximately to 11.1 N RMS), revealing typical stochastic nonlinear distortions and a shift of the resonance frequency of about 2 Hz.

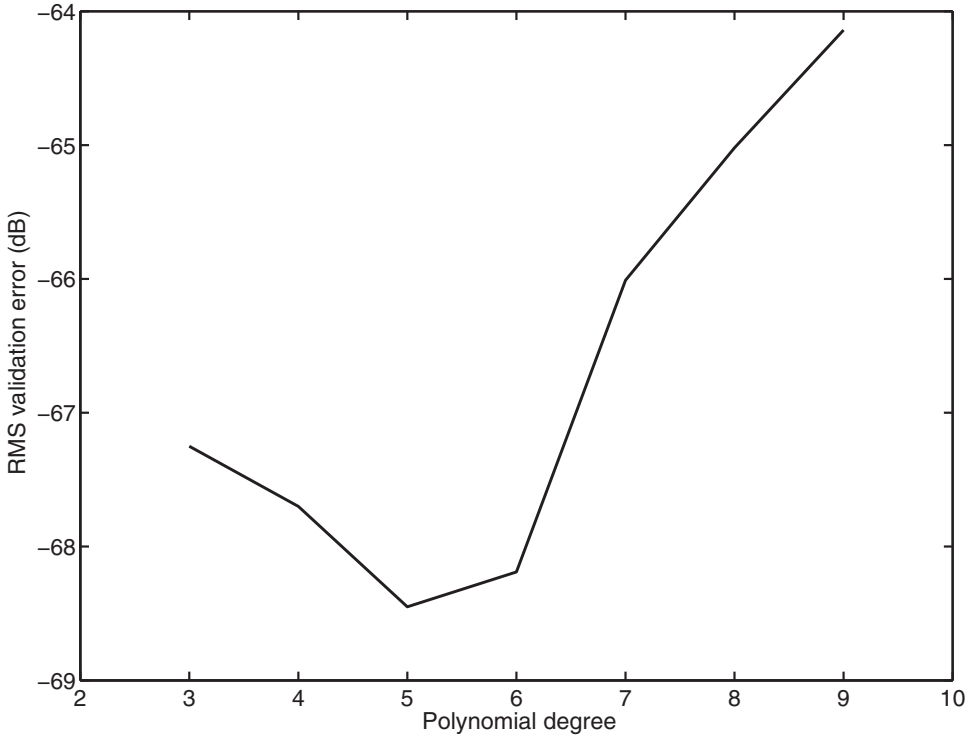

Figure 16. (Colour online) Time-domain RMS validation error for grey-box models with increasing polynomial degree.

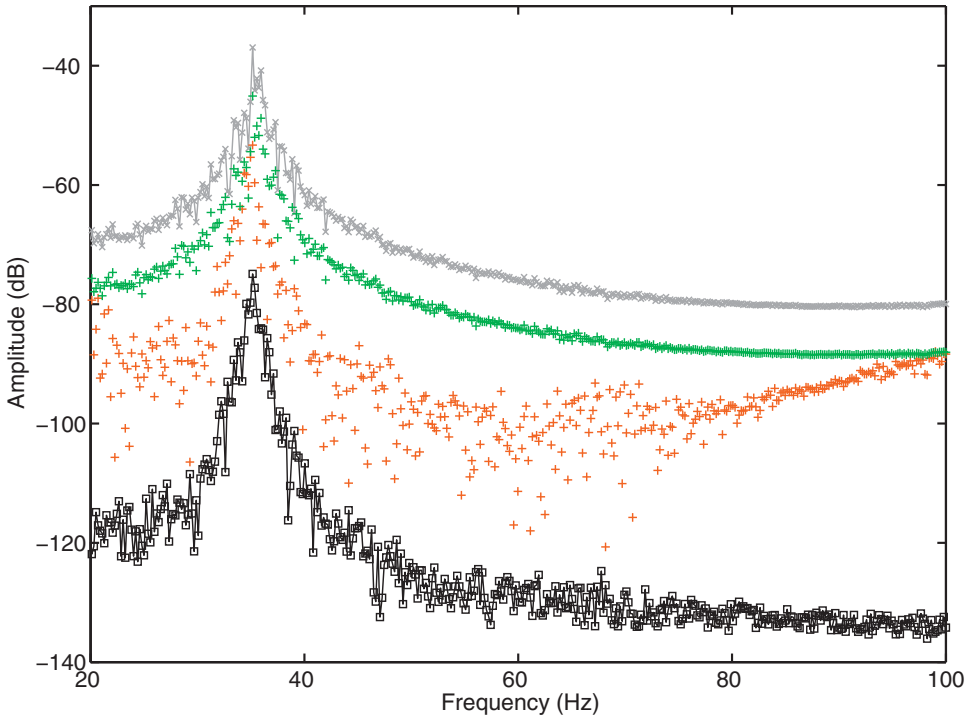

(a)

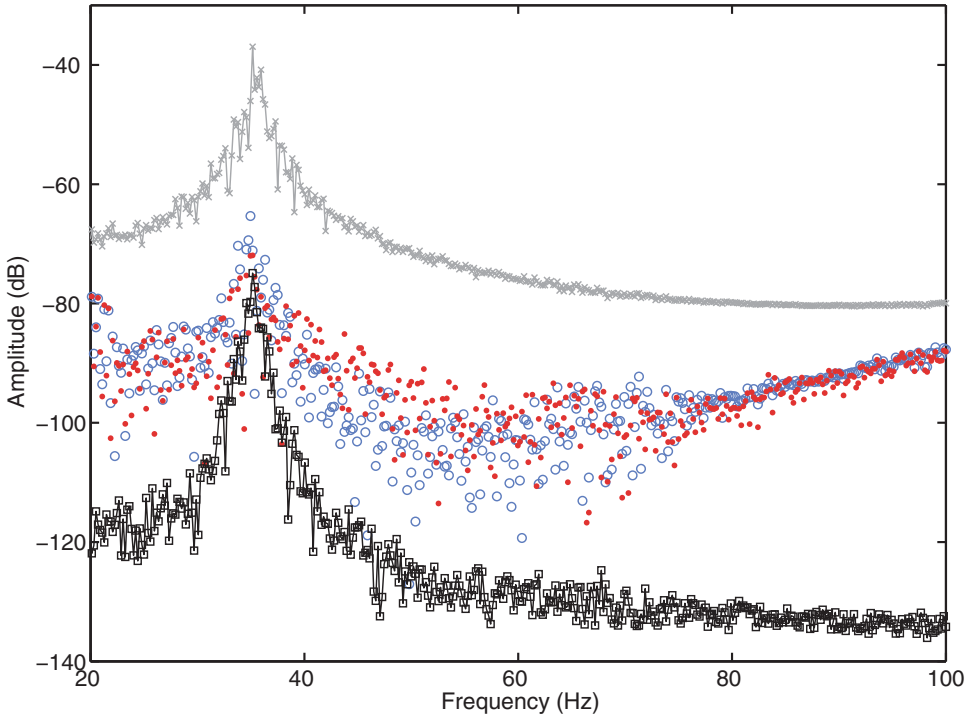

(b)

Figure 17. (Colour online) Frequency-domain comparison at sensor 7 of the grey-box and black-box state-space modelling approaches. Validation output spectra and noise levels are plotted in grey and black, respectively. (a) Initial grey-box model obtained using nonlinear subspace identification (in orange) and initial linear black-box model (in green); (b) final grey-box (in blue) and black-box (in red) models.

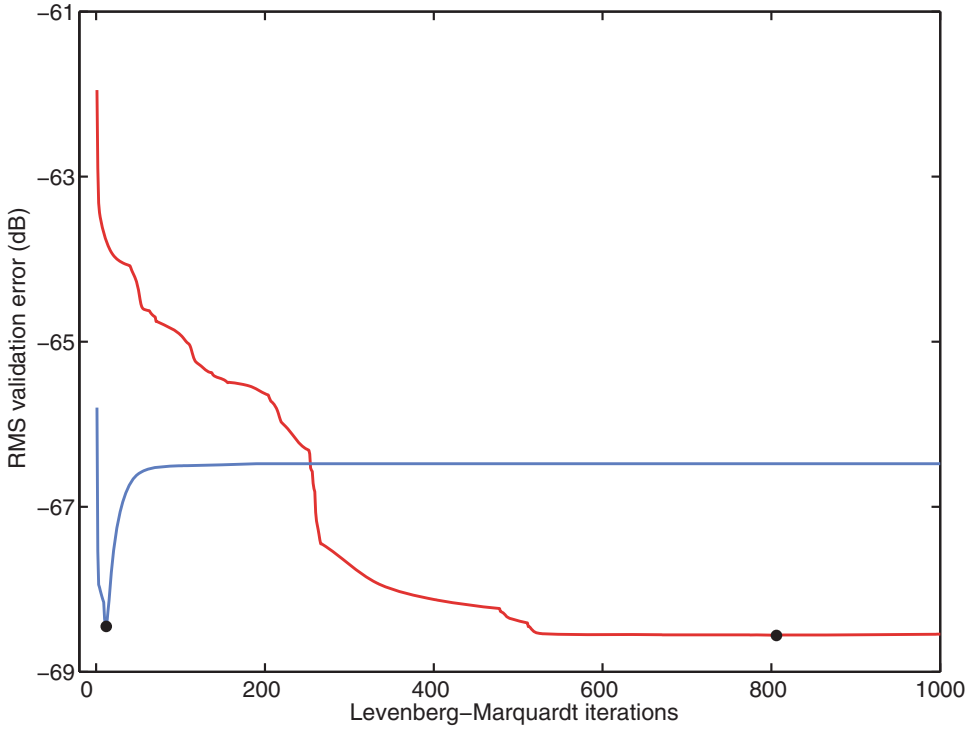

Figure 18. (Colour online) Decrease of the RMS validation error over 1000 Levenberg–Marquardt iterations for the grey-box (in blue) and black-box (in red) approaches. Optimal models are located using black dots.

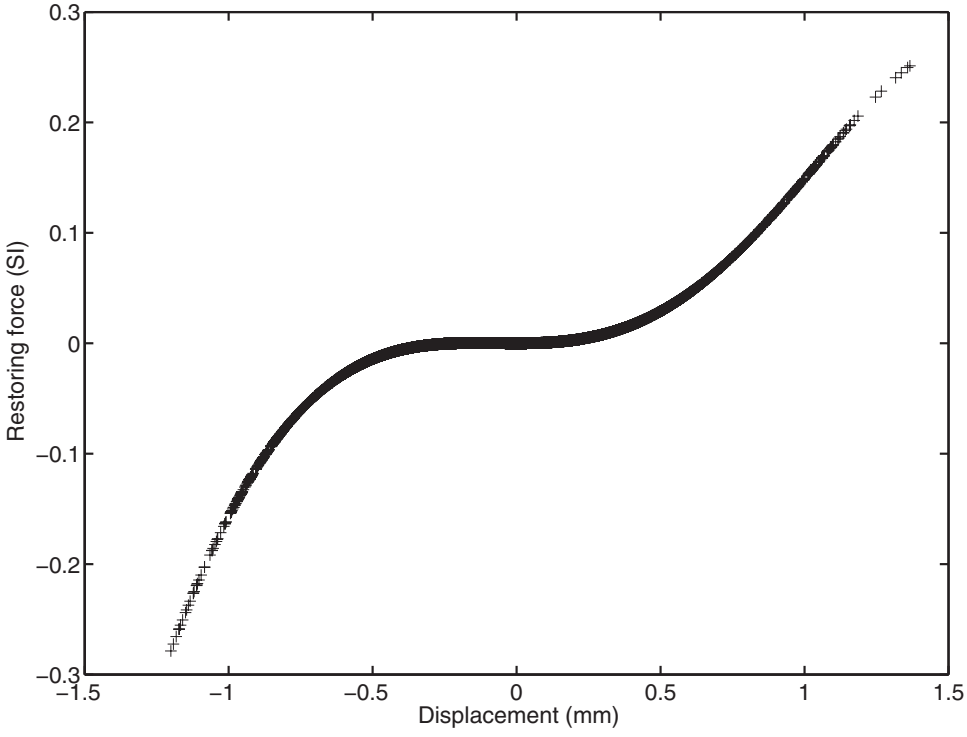

Figure 19. Physical restoring force of the nonlinear beam benchmark synthesised using the averaged nonlinear coefficients listed in Table 7.

Table 8. General comparison of the grey-box and black-box identification frameworks.

Grey-box state-space model	Black-box state-space model
Nonlinear model terms are univariate polynomials with a low number of parameters.	Nonlinear model terms are multivariate polynomials with a high number of parameters.
Nonlinear coefficients have physical meaning.	Nonlinear coefficients have no direct interpretation.
Identification procedure includes two steps with one nonlinear optimisation search.	Identification procedure includes four steps with two nonlinear optimisation searches.
Initialisation is based on a nonlinear subspace model.	Initialisation is based on a linearised model.

A grey-box model of the beam dynamics is constructed at 1.2 V RMS input amplitude considering nonlinear terms in the state equation formed using the displacement measured at the main beam tip (sensor number 7), i.e. the displacement measured at the nonlinearity location, denoted $y_{nl} = y_7$. A fifth-degree polynomial in y_{nl} is used to describe the geometrically nonlinear effects induced by the thin beam, leading to a second-order model in state-space comprising 35 parameters. Figure 15 presents validation model error plots in the frequency domain, featuring the output spectrum (in grey), initial (in orange) and final (in blue) grey-box state-space error levels, and noise level (in black). Two sensor locations are represented, namely (a) sensor 4 close to the mid-span of the main beam and (b) sensor 7 at the nonlinearity location. In the resonance region, the errors of the initial and final models are seen to lie about 15 and 30 dB below the output level, respectively. Out of resonance, initial and final model errors correspond and possess an amplitude larger than the noise floor. In Figure 16, the time-domain RMS validation error is plotted for grey-box models with increasing polynomial degree, showing a clear minimum corresponding to a representation of degree five.

In Figure 17, the obtained fifth-degree grey-box model is compared at sensor 7 with a black-box model including in the state equation a fifth-degree multivariate polynomial involving 36 monomial combinations of the two state variables, and resulting into a state-space model with 99 parameters. Similarly to the Silverbox analysis, Figure 17 shows that the initial grey-box model (in orange) provided by the nonlinear subspace identification algorithm outperforms the initial linear model (in green) of the black-box method. It is also observed that the two final models (grey-box in blue and black-box in red) achieve a comparable validation error level throughout the frequency band of interest, except in the vicinity of the system resonance, where the black-box model reaches the noise floor, 5 dB below the grey-box model error level. Finally, the study in Figure 18 of the Levenberg–Marquardt iterations necessary to achieve the final estimation of the state-space parameters reveals that optimal grey-box and black-box models are reached in 12 and 806 iterations, respectively.

The synthesis of the physical restoring force acting at the nonlinearity location, and expressed as the four-term sum $c_1\, y_{nl}^2(t) + c_2\, y_{nl}^3(t) + c_3\, y_{nl}^4(t) + c_4\, y_{nl}^5(t)$, is performed in Figure 19. The nonlinear coefficients in this expression were obtained by averaging over the 20–100 Hz band their frequency-dependent estimates generated as explained in Section 4.2. They are listed in Table 7. A dominant odd behaviour is noted in Figure 19, mainly associated with the cubic nonlinearity in the model. For positive displacements, an asymmetry is also remarked, visible as a softening of the force. This effect might be attributed to an imperfection in the clamping of the thin beam component, as already pointed out in Grappasonni, Noël, and Kerschen (2014).

6. Conclusions

The objective of the present paper was to introduce a grey-box state-space modelling framework to support the identification of nonlinear mechanical vibrations. Assuming nonlinearities localised in physical space, which is a generic case in mechanics, this framework was shown to pave the way for an important decrease in the number of parameters with respect to classical black-box state-space modelling. A general comparison of the grey-box and black-box identification features is drawn in Table 8.

The Silverbox benchmark was considered as a first experimental case study demonstrating the derived identification procedure, combining nonlinear subspace initialisation and weighted least-squares optimisation. Compared with nine other model structures, the proposed grey-box approach was shown to lead to a good compromise between fitting flexibility and parsimony. A nonlinear beam benchmark was treated as a second experimental case study, confirming the findings of the Silverbox analysis. Future research prospects include the application of the developed framework to multiple-mode and multiple-nonlinearity mechanical systems. The calculation of confidence bounds on the model parameters would be another major advance in the topic.

Disclosure statement

No potential conflict of interest was reported by the authors.

Funding

Fonds de la Recherche Scientifique – FNRS; Fund for Scientific Research-Flanders (FWO-Vlaanderen); the Flemish Government (Methusalem); the Belgian Government through the Inter University Poles of Attraction (IAP VII) Program; and the ERC Advanced Grant SNLSID [contract number 320378].

References

Ahlquist, J., Carreño, J., Climent, H., de Diego, R., & de Alba, J. (2010). Assessment of nonlinear structural response in A400M GVT. In *Proceedings of the 28th international modal analysis conference (IMAC)*. Jacksonville, FL: Society for Experimental Mechanics.

Antonio, D., Zanette, D., & Lopez, D. (2012). Frequency stabilization in nonlinear micromechanical oscillators. *Nature Communications*, *3*, 806.

Boechler, N., Theocharis, G., & Daraio, C. (2011). Bifurcation-based acoustic switching and rectification. *Nature Materials*, *10*, 665–668.

Carney, K., Yunis, I., Smith, K., & Peng, C. (1997). Nonlinear dynamic behavior in the Cassini spacecraft modal survey. In *Proceedings of the 15th international modal analysis conference (IMAC)*. Orlando, FL: Society for Experimental Mechanics.

Chen, H., Kurt, M., Lee, Y., McFarland, D., Bergman, L., & Vakakis, A. (2014). Experimental system identification of the dynamics of a vibro-impact beam with a view towards structural health monitoring and damage detection. *Mechanical Systems and Signal Processing*, *46*, 91–113.

Claeys, M., Sinou, J., Lambelin, J., & Alcoverro, B. (2014). Multi-harmonic measurements and numerical simulations of nonlinear vibrations of a beam with non-ideal boundary conditions. *Communications in Nonlinear Science and Numerical Simulation*, *19*, 4196–4212.

Grappasonni, C., Noël, J., & Kerschen, G. (2014). Subspace and nonlinear-normal-modes-based identification of a beam with softening-hardening behaviour. In *Proceedings of the 32nd international modal analysis conference (IMAC)*. Orlando, FL: Society for Experimental Mechanics.

Habib, G., & Kerschen, G. (2015). Suppression of limit cycle oscillations using the nonlinear tuned vibration absorber. *Proceedings of the Royal Society of London A*, *471*, 20140976.

Isasa, I., Hot, A., Cogan, S., & Sadoulet-Reboul, E. (2011). Model updating of locally non-linear systems based on multi-harmonic extended constitutive relation error. *Mechanical Systems and Signal Processing*, *25*, 2413–2425.

Karami, A., & Inman, D. (2012). Powering pacemakers from heartbeat vibrations using linear and nonlinear energy harvesting. *Applied Physics Letters*, *100*, 042901.

Laible, M., Fitzpatrick, K., & Grygier, M. (2013). International space station 2A array modal analysis. In *Proceedings of the 31st international modal analysis conference (IMAC)*. Garden Grove, CA: Society for Experimental Mechanics.

Levenberg, K. (1944). A method for the solution of certain problems in least squares. *Quarterly of Applied Mathematics*, *2*, 164–168.

Marchesiello, S., & Garibaldi, L. (2008). A time domain approach for identifying nonlinear vibrating structures by subspace methods. *Mechanical Systems and Signal Processing*, *22*, 81–101.

Marconato, A., Sjöberg, J., Suykens, J., & Schoukens, J. (2012). Identification of the Silverbox benchmark using nonlinear state-space models. In *Proceedings of the 16th symposium on system identification*. Brussels: International Federation of Automatic Control.

Marquardt, D. (1963). An algorithm for least-squares estimation of nonlinear parameters. *Journal of the Society for Industrial and Applied Mathematics*, *11*(2), 431–441.

Noël, J., & Kerschen, G. (2013). Frequency-domain subspace identification for nonlinear mechanical systems. *Mechanical Systems and Signal Processing*, *40*, 701–717.

Noël, J., & Kerschen, G. (2017). Nonlinear system identification in structural dynamics: 10 more years of progress. *Mechanical Systems and Signal Processing*, *83*, 2–35.

Noël, J., Renson, L., Grappasonni, C., & Kerschen, G. (2016). Identification of nonlinear normal modes of engineering structures under broadband forcing. *Mechanical Systems and Signal Processing*, *74*, 95–110.

Noël, J., Schoukens, J., & Kerschen, G. (2015). Grey-box nonlinear state-space modelling for mechanical vibrations identification. In *Proceedings of the 17th symposium on system identification*. Beijing: International Federation of Automatic Control.

Paduart, J., Lauwers, L., Swevers, J., Smolders, K., Schoukens, J., & Pintelon, R. (2010). Identification of nonlinear systems using polynomial nonlinear state space models. *Automatica*, *46*, 647–656.

Peeters, M., Kerschen, G., & Golinval, J. (2011). Dynamic testing of nonlinear vibrating structures using nonlinear normal modes. *Journal of Sound and Vibration*, *330*, 486–509.

Pintelon, R., & Schoukens, J. (2001). *System identification: A frequency domain approach*. Piscataway, NJ: IEEE Press.

Relan, R., & Schoukens, J. (2016). Recursive discrete-time models for continuous-time systems under band-limited assumptions. *IEEE Transactions on Instrumentation and Measurement*, *65*(3), 713–723.

Renson, L., Gonzalez-Buelga, A., Barton, D., & Neild, S. (2016). Robust identification of backbone curves using control-based continuation. *Journal of Sound and Vibration*, *367*, 145–158.

Schoukens, J., Nemeth, J., Crama, P., Rolain, Y., & Pintelon, R. (2003). Fast approximate identification of nonlinear systems. *Automatica*, *39*, 1267–1274.

Schoukens, J., Pintelon, R., & Rolain, Y. (1999). Study of conditional ML estimators in time and frequency-domain system identification. *Automatica*, *35*, 91–100.

Strachan, B., Shaw, S., & Kogan, O. (2013). Subharmonic resonance cascades in a class of coupled resonators. *Journal of Computation and Nonlinear Dynamics*, *8*(4), 041015.

Thouverez, F. (2003). Presentation of the ECL benchmark. *Mechanical Systems and Signal Processing*, *17*(1), 195–202.

Wierschem, N., Hubbard, S., Luo, J., Fahnestock, L., Spencer, B., McFarland, D., … Bergman, L. (2017). Response attenuation in a large-scale structure subjected to blast excitation utilizing a system of essentially nonlinear vibration absorbers. *Journal of Sound and Vibration*, *389*, 52–72.

Appendices

Appendix 1. Frequency-domain nonlinear subspace identification (FNSI) method

This appendix details the FNSI algorithm (Noël & Kerschen, 2013) used in Section 3.1 to derive non-iteratively from data initial estimates of the matrices $(\mathbf{A}, \overline{\mathbf{B}}, \mathbf{C}, \overline{\mathbf{D}})$ in Equation (7).

The measured output spectra are first organised in a complex-valued matrix $\mathbf{Y}_i^c$ defined as

$$\mathbf{Y}_i^c = \begin{pmatrix} \mathbf{Y}(1) & \mathbf{Y}(2) & \dots & \mathbf{Y}(F) \\ z_1\,\mathbf{Y}(1) & z_2\,\mathbf{Y}(2) & \dots & z_F\,\mathbf{Y}(F) \\ z_1^2\,\mathbf{Y}(1) & z_2^2\,\mathbf{Y}(2) & \dots & z_F^2\,\mathbf{Y}(F) \\ \vdots & & & \\ z_1^{i-1}\,\mathbf{Y}(1) & z_2^{i-1}\,\mathbf{Y}(2) & \dots & z_F^{i-1}\,\mathbf{Y}(F) \end{pmatrix} \in \mathbb{C}^{li\times F}, \tag{A1}$$

where the superscript c stands for *complex*, and the subscript i is the user-defined number of block rows in $\mathbf{Y}_i^c$. The number of processed frequency lines is noted F and the number of output variables is l. Defining $\zeta = \mathrm{diag}\,(z_1\ z_2\ \cdots\ z_F) \in \mathbb{C}^{F\times F}$ and grouping frequency lines, $\mathbf{Y}_i^c$ is recast into

$$\mathbf{Y}_i^c = \begin{pmatrix} \mathbf{Y} \\ \mathbf{Y}\,\zeta \\ \mathbf{Y}\,\zeta^2 \\ \dots \\ \mathbf{Y}\,\zeta^{i-1} \end{pmatrix}. \tag{A2}$$

The matrix of the extended input spectra is similarly formed as

$$\overline{\mathbf{U}}_i^c = \begin{pmatrix} \overline{\mathbf{U}} \\ \overline{\mathbf{U}}\,\zeta \\ \overline{\mathbf{U}}\,\zeta^2 \\ \dots \\ \overline{\mathbf{U}}\,\zeta^{i-1} \end{pmatrix} \in \mathbb{C}^{(m+sl)\,i\times F}, \tag{A3}$$

where m is the number of extended input variables. Introducing the extended observability matrix

$$\mathbf{\Gamma}_i = \begin{pmatrix} \mathbf{C} \\ \mathbf{CA} \\ \mathbf{CA}^2 \\ \dots \\ \mathbf{CA}^{i-2} \\ \mathbf{CA}^{i-1} \end{pmatrix} \in \mathbb{R}^{li\times n_s} \tag{A4}$$

and the lower block triangular Toeplitz matrix $\mathbf{\Lambda}_i$

$$\mathbf{\Lambda}_i = \begin{pmatrix} \overline{\mathbf{D}} & \mathbf{0} & \mathbf{0} & \dots\ \mathbf{0} \\ \mathbf{C}\overline{\mathbf{B}} & \overline{\mathbf{D}} & \mathbf{0} & \dots\ \mathbf{0} \\ \mathbf{CA}\overline{\mathbf{B}} & \mathbf{C}\overline{\mathbf{B}} & \overline{\mathbf{D}} & \dots\ \mathbf{0} \\ \vdots & \vdots & \vdots & \vdots \\ \mathbf{CA}^{i-2}\overline{\mathbf{B}} & \mathbf{CA}^{i-3}\overline{\mathbf{B}} & \mathbf{CA}^{i-4}\overline{\mathbf{B}} & \dots\ \overline{\mathbf{D}} \end{pmatrix} \in \mathbb{R}^{li\times(m+sl)\,i}, \tag{A5}$$

recursive substitution of the second relation into the first relation of Equation (7) results in the output-state–input relationship

$$\mathbf{Y}_i^c = \mathbf{\Gamma}_i\,\mathbf{X}^c + \mathbf{\Lambda}_i\,\overline{\mathbf{U}}_i^c, \tag{A6}$$

where $\mathbf{X}^c \in \mathbb{C}^{n_s\times F}$ is the state spectrum. To force the identified state-space model $(\mathbf{A}, \overline{\mathbf{B}}, \mathbf{C}, \overline{\mathbf{D}})$ to be real-valued, Equation (A6) is finally converted into the real equation

$$\mathbf{Y}_i = \mathbf{\Gamma}_i\,\mathbf{X} + \mathbf{\Lambda}_i\,\overline{\mathbf{U}}_i \tag{A7}$$

by separating the real and imaginary parts of $\mathbf{Y}_i^c$, $\mathbf{X}^c$ and $\overline{\mathbf{U}}_i^c$, for instance,

$$\mathbf{Y}_i = \left[\mathcal{R}(\mathbf{Y}_i^c)\ \mathcal{I}(\mathbf{Y}_i^c)\right] \in \mathbb{R}^{li\times 2F}, \tag{A8}$$

where $\mathcal{R}$ and $\mathcal{I}$ denote the real and imaginary parts, respectively.

Under the assumptions discussed in Noël and Kerschen (2013), the orthogonal projection $\mathbf{O}_i = \mathbf{Y}_i/\overline{\mathbf{U}}_i^{\perp}$ and its singular value decomposition $\mathbf{O}_i = \mathbf{L}\,\mathbf{S}\,\mathbf{R}^T$ are computed. An estimate of the extended observability matrix $\mathbf{\Gamma}_i$ can then be shown to be given by

$$\widehat{\mathbf{\Gamma}}_i = \mathbf{L}_1\,\mathbf{S}_1^{1/2}, \tag{A9}$$

where $\mathbf{L}_1$ and $\mathbf{S}_1$ contain the first n_s left singular vectors and singular values of $\mathbf{O}_i$, respectively, and where hat symbols signal estimated quantities. From Equation (A9), $\widehat{\mathbf{C}}$ is merely extracted as the l first rows of $\widehat{\mathbf{\Gamma}}_i$. An estimate of $\mathbf{A}$ can be calculated by exploiting the shift property

$$\underline{\mathbf{\Gamma}_i}\,\mathbf{A} = \overline{\mathbf{\Gamma}_i}, \tag{A10}$$

where $\underline{\mathbf{\Gamma}_i}$ and $\overline{\mathbf{\Gamma}_i}$ are the matrix $\widehat{\mathbf{\Gamma}}_i$ without its last and first l rows, respectively. Matrix $\mathbf{A}$ is therefore found as the least-squares solution

$$\widehat{\mathbf{A}} = \underline{\mathbf{\Gamma}_i}^{\dagger}\,\overline{\mathbf{\Gamma}_i}, \tag{A11}$$

where the symbol † denotes the pseudo-inverse operation.

Given estimates of $\mathbf{A}$ and $\mathbf{C}$, matrices $\overline{\mathbf{B}}$ and $\overline{\mathbf{D}}$ are finally obtained by defining the transfer function matrix $\mathbf{G}_s$ associated with Equation (7) as

$$\mathbf{G}_s(k) = \widehat{\mathbf{C}}\left(z_k\,\mathbf{I}^{n_s\times n_s} - \widehat{\mathbf{A}}\right)^{-1}\overline{\mathbf{B}} + \overline{\mathbf{D}}, \tag{A12}$$

and by minimising the difference between the measured and modelled output spectra in a linear least-squares sense, i.e.

$$\widehat{\overline{\mathbf{B}}}, \widehat{\overline{\mathbf{D}}} = \arg\min_{\overline{\mathbf{B}},\overline{\mathbf{D}}} \sum_{k=1}^{F} \left|\mathbf{Y}(k) - \mathbf{G}_s(k)\overline{\mathbf{U}}(k)\right|^2. \tag{A13}$$

Appendix 2. Analytical calculation of the Jacobian matrix

One first focuses on the determination of the element $J_{A_{ij}}(t) \in \mathbb{R}^l$ of the time-domain Jacobian defined as

$$J_{A_{ij}}(t) = \frac{\partial \mathbf{y}(t)}{\partial A_{ij}}. \tag{B1}$$

The derivative of the output relation in Equation (6) with respect to A_{ij} is given by

$$\begin{aligned}\frac{\partial \mathbf{y}(t)}{\partial A_{ij}} &= \frac{\partial}{\partial A_{ij}}\left(\mathbf{C}\,\mathbf{x}(t) + \overline{\mathbf{D}}\,\overline{\mathbf{u}}(t)\right)\\ &= \mathbf{C}\,\frac{\partial \mathbf{x}(t)}{\partial A_{ij}} + \overline{\mathbf{D}}\,\frac{\partial \overline{\mathbf{u}}(t)}{\partial A_{ij}}\\ &= \mathbf{C}\,\frac{\partial \mathbf{x}(t)}{\partial A_{ij}} + \overline{\mathbf{D}}\,\frac{\partial \overline{\mathbf{u}}(t)}{\partial \mathbf{y}(t)}\frac{\partial \mathbf{y}(t)}{\partial A_{ij}}.\end{aligned} \tag{B2}$$

The first term in the right-hand side of Equation (B2) is obtained by taking the derivative of the state relation in Equation (6) with respect to A_{ij}, that is

$$\begin{aligned}\frac{\partial \dot{\mathbf{x}}(t)}{\partial A_{ij}} &= \frac{\partial}{\partial A_{ij}}\left(\mathbf{A}\,\mathbf{x}(t) + \overline{\mathbf{B}}\,\overline{\mathbf{u}}(t)\right)\\ &= \mathbf{A}\,\frac{\partial \mathbf{x}(t)}{\partial A_{ij}} + \mathbf{I}_{ij}^{n_s\times n_s}\,\mathbf{x}(t) + \overline{\mathbf{B}}\,\frac{\partial \overline{\mathbf{u}}(t)}{\partial A_{ij}}\\ &= \mathbf{A}\,\frac{\partial \mathbf{x}(t)}{\partial A_{ij}} + \mathbf{I}_{ij}^{n_s\times n_s}\,\mathbf{x}(t) + \overline{\mathbf{B}}\,\frac{\partial \overline{\mathbf{u}}(t)}{\partial \mathbf{y}(t)}\frac{\partial \mathbf{y}(t)}{\partial A_{ij}},\end{aligned} \tag{B3}$$

where $\mathbf{I}_{ij}^{n_s\times n_s}$ is a zero matrix with a single element equal to one at entry (i, j).

The element $J_{A_{ij}}(t)$ is therefore given by the solution of the two equations

$$\begin{cases}\dfrac{\partial \dot{\mathbf{x}}(t)}{\partial A_{ij}} = \mathbf{A}\,\dfrac{\partial \mathbf{x}(t)}{\partial A_{ij}} + \mathbf{I}_{ij}^{n_s\times n_s}\,\mathbf{x}(t) + \overline{\mathbf{B}}\,\dfrac{\partial \overline{\mathbf{u}}(t)}{\partial \mathbf{y}(t)}\dfrac{\partial \mathbf{y}(t)}{\partial A_{ij}}\\ \dfrac{\partial \mathbf{y}(t)}{\partial A_{ij}} = \mathbf{C}\,\dfrac{\partial \mathbf{x}(t)}{\partial A_{ij}} + \overline{\mathbf{D}}\,\dfrac{\partial \overline{\mathbf{u}}(t)}{\partial \mathbf{y}(t)}\dfrac{\partial \mathbf{y}(t)}{\partial A_{ij}}.\end{cases} \tag{B4}$$

Introducing the notations

$$\begin{aligned}\mathbf{x}^*(t) = \frac{\partial \mathbf{x}(t)}{\partial A_{ij}}\,;\ \mathbf{y}^*(t) = \tfrac{\partial \mathbf{y}(t)}{\partial A_{ij}}\,;\\ \overline{\mathbf{u}}^*(t) = \left(\mathbf{x}(t)^T\left(\frac{\partial \overline{\mathbf{u}}(t)}{\partial \mathbf{y}(t)}\frac{\partial \mathbf{y}(t)}{\partial A_{ij}}\right)^T\right)^T\end{aligned} \tag{B5}$$

and

$$\begin{aligned}\mathbf{A}^* = \mathbf{A}\,;\ \overline{\mathbf{B}}^* = \left(\mathbf{I}_{ij}^{n_s\times n_s}\ \overline{\mathbf{B}}\right);\\ \mathbf{C}^* = \mathbf{C};\ \overline{\mathbf{D}}^* = \left(\mathbf{0}^{l\times n_s}\ \overline{\mathbf{D}}\right),\end{aligned} \tag{B6}$$

Equation (B4) can be recast in the form

$$\begin{cases}\dot{\mathbf{x}}^*(t) = \mathbf{A}^*\,\mathbf{x}^*(t) + \overline{\mathbf{B}}^*\,\overline{\mathbf{u}}^*(t)\\ \mathbf{y}^*(t) = \mathbf{C}^*\,\mathbf{x}^*(t) + \overline{\mathbf{D}}^*\,\overline{\mathbf{u}}^*(t).\end{cases} \tag{B7}$$

Equation (B7) reveals that the elements of the Jacobian matrix associated with the parameters in $\mathbf{A}$ are solutions of an auxiliary state-space model defined by the four matrices $(\mathbf{A}^*, \overline{\mathbf{B}}^*, \mathbf{C}^*, \overline{\mathbf{D}}^*)$. The first term in the auxiliary extended input $\overline{\mathbf{u}}^*(t)$ in Equation (B5) is the state vector $\mathbf{x}(t)$. It is obtained by simulating in time the original model in Equation (6) with the estimated parameters of the previous Levenberg–Marquardt iteration. The second term in $\overline{\mathbf{u}}^*(t)$ depends on $\partial\overline{\mathbf{u}}(t)/\partial\mathbf{y}(t)$, which is formed using the derivatives of the nonlinear basis functions $\mathbf{g}(\mathbf{y}_{nl}(t), \dot{\mathbf{y}}_{nl}(t))$ with respect to $\mathbf{y}(t)$.

The determination of the element $J_{\overline{B}_{ij}}(t) \in \mathbb{R}^l$ is conducted similarly to $J_{A_{ij}}(t)$. The result is given in Equation (B8), where $J_{\overline{B}_{ij}}(t)$ is seen to be the solution of another auxiliary state-space model,

$$\begin{cases}\dfrac{\partial \dot{\mathbf{x}}(t)}{\partial \overline{B}_{ij}} = \mathbf{A}\,\dfrac{\partial \mathbf{x}(t)}{\partial \overline{B}_{ij}} + \mathbf{I}_{ij}^{n_s\times(m+sl)}\,\overline{\mathbf{u}}(t) + \overline{\mathbf{B}}\,\dfrac{\partial \overline{\mathbf{u}}(t)}{\partial \mathbf{y}(t)}\dfrac{\partial \mathbf{y}(t)}{\partial \overline{B}_{ij}}\\ \dfrac{\partial \mathbf{y}(t)}{\partial \overline{B}_{ij}} = \mathbf{C}\,\dfrac{\partial \mathbf{x}(t)}{\partial \overline{B}_{ij}} + \overline{\mathbf{D}}\,\dfrac{\partial \overline{\mathbf{u}}(t)}{\partial \mathbf{y}(t)}\dfrac{\partial \mathbf{y}(t)}{\partial \overline{B}_{ij}}.\end{cases} \tag{B8}$$

The computation of $J_{C_{ij}}(t) \in \mathbb{R}^l$ and $J_{\overline{D}_{ij}}(t) \in \mathbb{R}^l$ is easier because they do not involve time integration, as shown in Equations (B9) and (B10), respectively,

$$\frac{\partial \mathbf{y}(t)}{\partial C_{ij}} = \mathbf{I}_{ij}^{l\times n_s}\,\mathbf{x}(t) + \overline{\mathbf{D}}\,\frac{\partial \overline{\mathbf{u}}(t)}{\partial \mathbf{y}(t)}\,\frac{\partial \mathbf{y}(t)}{\partial C_{ij}}; \tag{B9}$$

$$\frac{\partial \mathbf{y}(t)}{\partial \overline{D}_{ij}} = \mathbf{I}_{ij}^{l\times (m+sl)}\,\overline{\mathbf{u}}(t) + \overline{\mathbf{D}}\,\frac{\partial \overline{\mathbf{u}}(t)}{\partial \mathbf{y}(t)}\,\frac{\partial \mathbf{y}(t)}{\partial \overline{D}_{ij}}. \tag{B10}$$